LAWRENCE
LIVERMORE
NATIONAL
LABORATORY

UCRL-TR-218582

FY2004 Progress Summary and FY2005 Program Plan Statement of Work and Deliverables

W. Meier and C. Bibeau

January 2006

This work was performed under the auspices of the U.S. Department of Energy by University of California, Lawrence Livermore National Laboratory under Contract W-7405-Eng-48.

FY2004 Progress Summary
and
FY2005 Program Plan
Statement of Work and Deliverables

For

Development of High Average Power Diode-Pumped Solid State Lasers, and Complementary Technologies, for Applications in Energy and Defense

Presented to
Dr. Tom Finn, DP/DOE,
Virtual Office of Inertial Fusion Energy

Continuation of DOE Contract Number DE-AI03-94SF19892

Document release 1.7

For further information contact:

Dr. Wayne Meier
Deputy Program Leader for IFE
Phone: (925) 422-8536
meier5@llnl.gov
or
Dr. Camille Bibeau
Project Leader for Mercury Laser
Phone: (925) 422-7798
bibeau1@llnl.gov

Lawrence Livermore National Laboratory
Livermore, CA 94550

TABLE OF CONTENTS

FY2004 PROGRESS SUMMARY

TABLE OF CONTENTS

2.1 DPSSL Development

2.1.1 Executive Summary: Mercury Laser

Our main goal was to validate the integrated operation of the laser with two amplifiers pumped by eight diode arrays. The system was operated for extended run periods which enabled average power testing of components, diagnostics, and controls. These tests were highly successful, with a demonstrated energy level of over 35 joules for 4 hours at a repetition rate of 3.5 Hz. This is equivalent to the level previously achieved with the single amplifier before the system was commissioned with two amplifiers. Plans to achieve higher energy levels and average power are in progress.

The dual amplifier system is employed in a 4-pass arrangement. The Yb:S-FAP slabs were mounted in aerodynamic aluminum vane structures to allow turbulent helium gas flow across the faces. Diagnostic packages including a damage detection sensor were deployed during operation. The experiments involved sending an injection beam through the amplifier and optical train in a 4-pass angularly multiplexed alignment scheme. In order to correct for static phase distortions incurred during crystal fabrication, a custom-designed magneto-rheologically-finished (MRF) phase-corrector-plate was fabricated and installed. The corrector plate improved the output beam quality to a point where that 96% of the energy was inside a 5 times diffraction limited spot.

A picture of the laser system with amplifier 2 (foreground) and amplifier 1 (background) is shown in Fig. 2.1.1.1. The control system and diagnostics have been upgraded to allow parallel processing and remote administration of operations. Initial commissioning of the diagnostic and control systems was successful.

Figure 2.1.1.1 Photograph of the two amplifier Mercury laser laboratory

The growth and fabrication of the Yb:S-FAP slabs constituted another major element of our program objectives. Our goal was to produce at least seven 4x6 cm^2 crystalline slabs. Seven

crystals were successfully fabricated and installed in the system while four are currently in fabrication. Twelve crystalline boules are currently in the production queue. A major improvement to the fabrication process was attained by changing to a water jet cutting process and a new cutting geometry. Results thus far indicate a factor of two improvement in the yield with these new techniques. Growth efforts at Northrop-Grumman, our industrial collaborator, resulted in the production of five 6.5 cm diameter boules (compared to the previous growth diameter of 3.5 cm). These represent the first large diameter Yb:S-FAP boules to be grown with the Czochralski method. We are encouraged by these results and are fine-tuning the process using methods previously developed for smaller boules to eliminate the index variations (striae). The LLNL effort has been focused on producing smaller diameter, but higher quality boules. These boules yielded half size slabs that were bonded together with a high temperature process to form full size parts. The bonding process gives rise to wavefront distortions directly along the bond region. However, better alignment and deterministic polishing methods are being pursued to eliminate these distortions. In the final configuration, the Mercury laser will require a total of 14 laser slabs. A dual approach comprised of an experimental crystal growth research facility at LLNL along with a commercial vendor using established protocols for production crystal growth, appears to be a good model. A similar approach was adopted as part of the National Ignition Facility KDP crystal production process.

The remaining diode bars needed to pump a second amplifier assembly were purchased from Coherent Inc. and packaged at LLNL using state of the art technology required to cool the diode bars and maintain the stringent requirements pertaining to peak power, bandwidth, wavelength chirp, and reliability. This year over 140, 23-diode-bar packages were fabricated and mounted on a copper-cooled block referred to as a backplane. Each backplane produced 80 kW of peak power. The pulse power units were modified by the manufacturer to improve performance and were subsequently operated at LLNL using a computer-controlled system.

The following sections discuss the above accomplishments in more technical detail and are followed by plans and a budget request for FY2005.

2.1.2 Architecture

The conceptual layout for the full laser design is shown in Fig. 2.1.2.1. The layout incorporates an angularly multiplexed beam path. The front-end laser is injected off-axis into the first amplifier. After the beam passes through the second amplifier, it is reflected from the end mirror and returns to a different focus location (see image inset). A set of mirrors in the "beam reverser" path are used to re-inject the beam into the amplifier chain for two additional passes resulting in a total of 4 passes through the system. Several telescopes are used to relay a spatially smooth beam profile from amplifier to amplifier to reduce beam modulation (Fig. 2.1.2.2). A Pockels cell is be located in the reverser path to reject parasitic reflections.

The amplifier is optically pumped from both sides by the diode arrays. The dual-ended pumping design helps to smooth the pump profiles and thermal loading on the crystals. The light from the diode array is concentrated with hollow reflective optics that homogenize the spatial profile of the pump beam. The optics are coated on the inside surfaces with silver coatings that have high reflectivity (greater than 99%) at grazing incidence angles. Over 80% of the diode light is reaches the first amplifier slab. Each of the seven amplifier slabs (Fig. 2.1.2.3a) are mounted or potted into aerodynamic aluminum vane elements as shown in Fig. 2.1.2.3b. The seven vanes are precision mounted within a helium gas flow assembly.

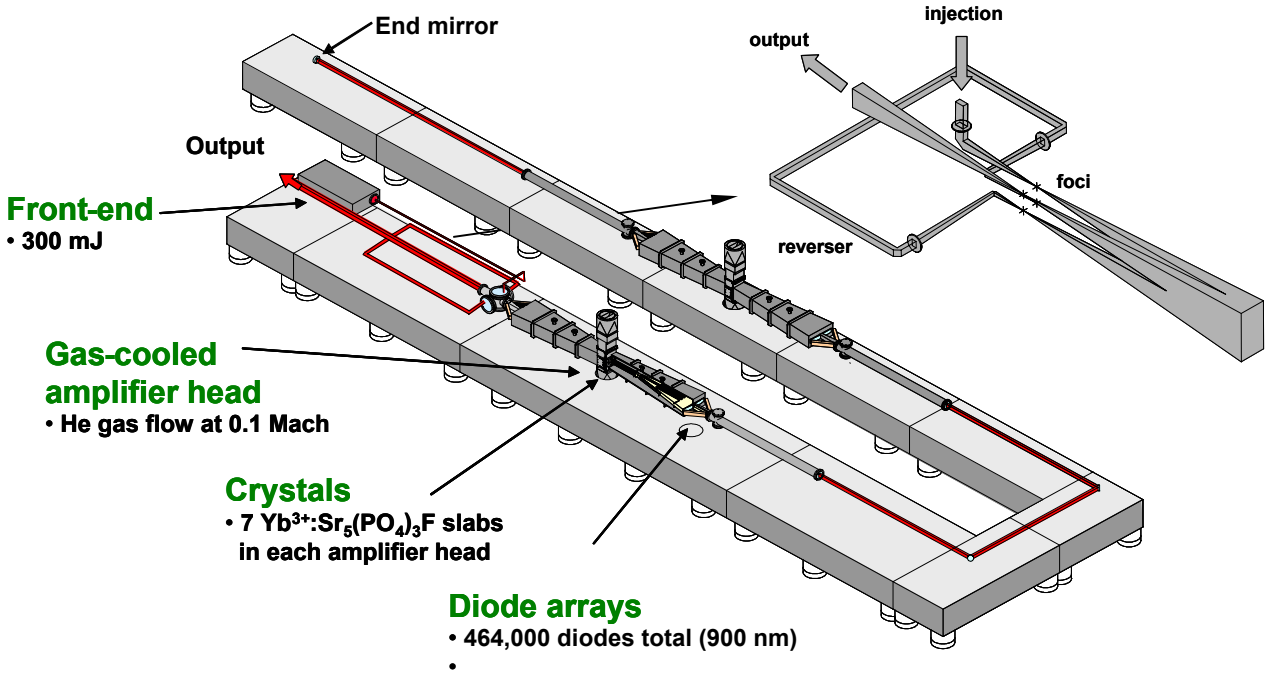

Fig. 2.1.2.1 Mercury laser system layout and enlargement of injection and reverser system.

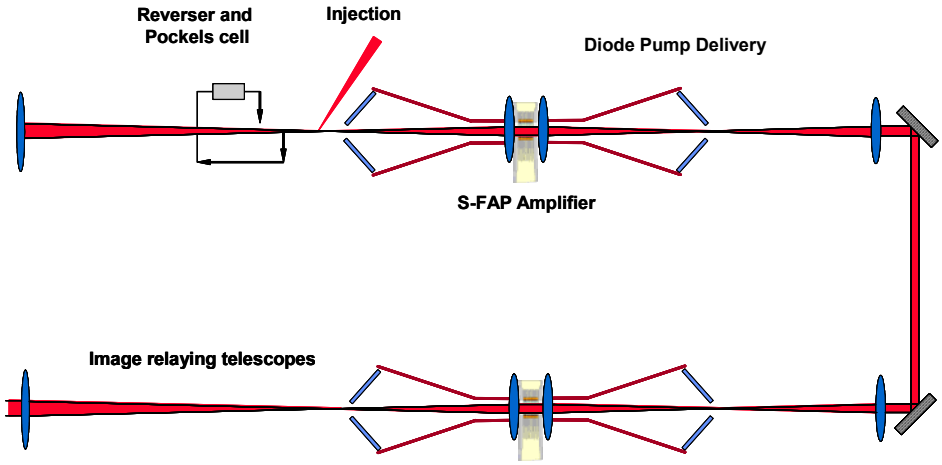

Fig. 2.1.2.2 Schematic top view of the optical layout.

(a) 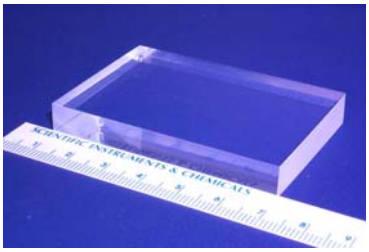 (b) 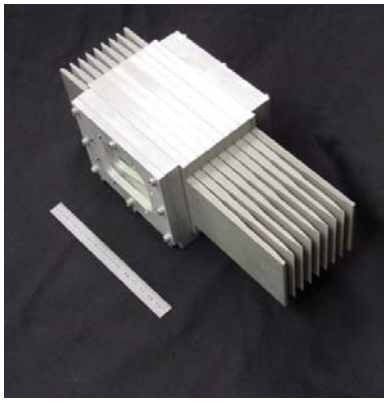

Fig. 2.1.2.3 (a) Yb:S-FAP slab, (b) Aluminum vanes

The diode pump arrays on either side of the amplifier consist of two 6x6 arrays of tiles. The arrays emit light with a divergence of 0.8x8 degrees. The laser beam passes through the space between the arrays shown on the left side of Fig. 2.1.2.4. The diode pump delivery and laser beam optics are coupled, allowing the pump-amplifier module to be quite compact. Modeling is required for stray light analysis to track unwanted reflections.

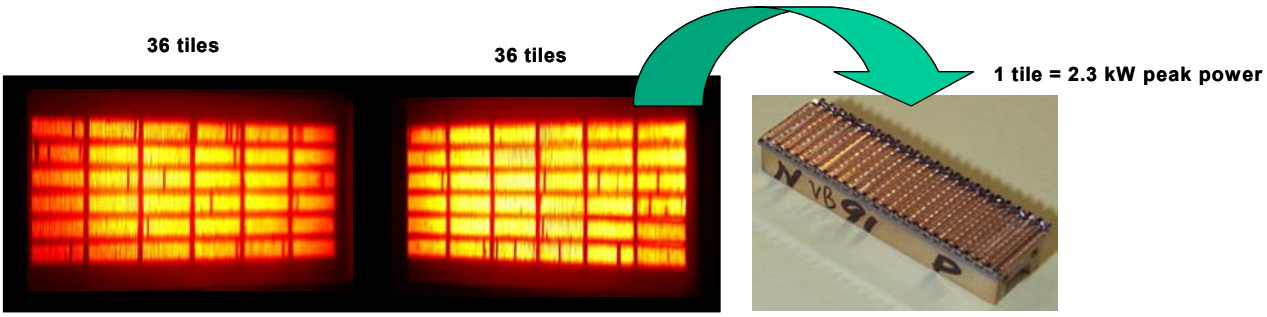

Fig. 2.1.2.4 Image of diode arrays firing producing up to 160 kW of peak power at 900 nm.

2.1.3 Controls System and Diagnostics

Since the deployment of the Mercury system in FY2002, the diagnostics have evolved toward more automated operation. Several additions were developed including the midfield camera, bright-field diagnostic, and diode array cameras. The midfield camera uses a 12-bit, 2 mega-pixel, 10 Hz images after two passes for live monitoring of the near-field beam quality. The bright-field diagnostic captures the near-field to assess damage in the reverser and other out-of-relay optics. Diffraction from damage on out-of-relay optics typically leads to large-scale modulation observed as “holes” in the intensity profile. Using beam analysis software, the control system quickly processes the image and safely shuts down the laser within one shot after detection of optical damage. Another diagnostic was developed to directly monitor the diode “tiles” during operation. This system provides the additional capability to halt system operation if a diode fault condition or malfunction is detected.

2.1.4 Mercury Computer Control System

The Mercury Control System has been used for approximately 380,000 shots on each of the eight diode arrays, pulsers and power supplies driving them. The data in Figure 2.1.4.1 shows the accumulated shot totals for FY 2004.

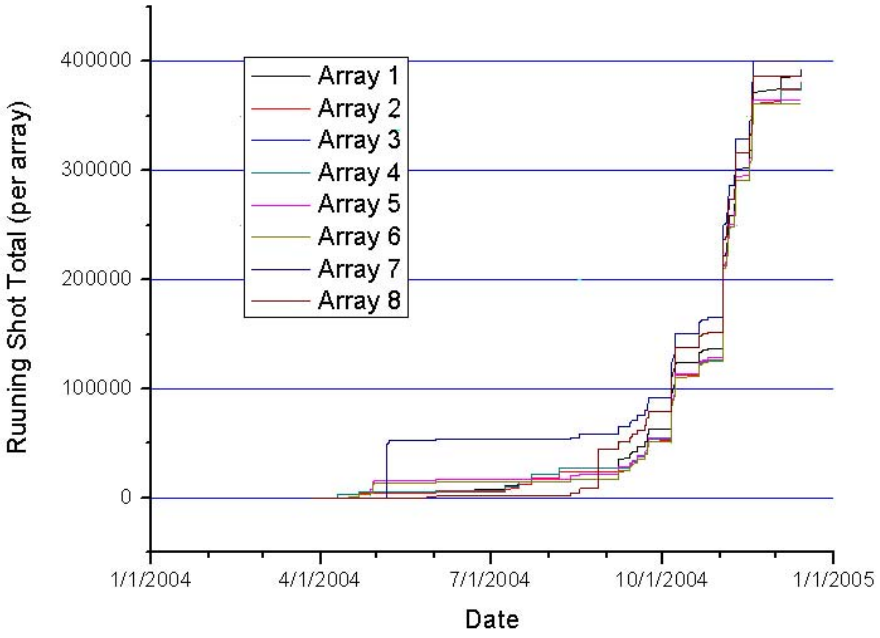

Fig. 2.1.4.1 The accumulated shot total of the diode laser array and diode pulsers.

The diode pulsers have been operating for approximately one year and are proving to be very robust units. The principal issue with the control system components was found to be the relays in the programmable logic controller (PLC), which provide the permissives to the pulsers. These relays were not sealed units. The electrical contacts of the relays oxidized in the time since the relays were installed. To remedy this problem, the relays were replaced with sealed units.

With the addition of a second PLC, the computer interface to the Safety Interlock System (SIS) was replaced with a newer unit containing a faster processor, more memory and a flat panel display. This change increased the user response time of the system. We have added controls and interlocks for the second amplifier chain, installed more reliable humidity sensors, and added beam tube interlocks

.

2.1.5 Laser Diodes

A total of 73 V-BASIS diode tiles where fabricated for the Mercury project. Thirty six of those of the tiles were mounted on a backplane (Fig. 2.1.5.1). The remaining 37 packages were inventoried as spare parts/


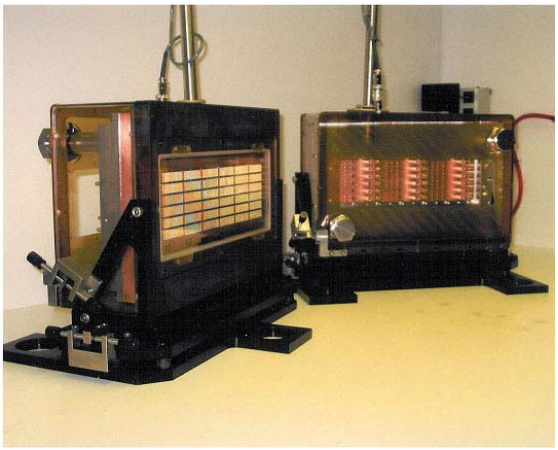

Fig. 2.1.5.1 A new diode array back plane was delivered in FY2004 as well as 37 individual V-BASIS packages for replacements or future use on a new back plane.

A cumulative total of 439 V-BASIS packages have been fabricated with performance goals described in Table 2.1.5.1.

Table 2.1.5.1 Diode performance goals and status

Design Goal	Status
< 10 nm FWHM at 750 us pulse	5 nm FWHM demonstrated
> 100 W peak output power per bar	Bars burned in at 115 W per bar
> 10% droop over pulse	5% droop demonstrated on 1 msec pulse
> 50% wall plug efficient	44% wall plug efficiency demonstrated
> 10:1 TE/TM polarization ratio	> 10:1 TE /TM polarization ratio
> 10^8 shot lifetime	1.4x10^8 shots

With the exception of the 50% wall plug efficiency, all of the specifications shown above have been successfully demonstrated and continue to be met. Of particular importance to the extraction, is that the laser diode bars have a very narrow wavelength distribution, enabling efficient coupling to the 900 nm Yb:S-FAP absorption feature. Fig. 2.1.5.2 is a histogram of the wavelength distribution of the 73 V-BASIS packages produced in FY2004, totaling 1,679 laser diode bars that were procured from Coherent Inc. Overlaid on the histogram of the diode bar emission wavelength is the spectrally resolved Yb:S-FAP absorption cross section showing the tolerance to which the diode bar wavelength was held. The mean wavelength of the diode bar distribution depicted in Fig. 2.1.5.2 is 900.6 nm with a standard deviation of 0.9 nm.

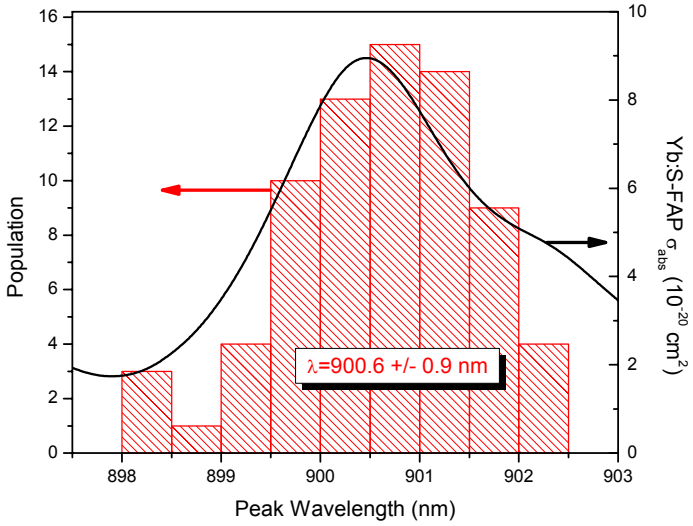

Fig. 2.1.5.2 A histogram showing the wavelength distribution of 1,679 diode bars. Also shown is the 900 nm Yb:S-FAP absorption feature, to which the diode radiation is coupled.

2.1.6 Czochralski Crystal Growth

The goals of the high temperature crystal growth effort are to produce high quality Yb:S-FAP [Yb^{3+}:$Sr_5(PO_4)_3F$] crystalline slabs. Each of the two amplifiers requires 7 slabs of dimension 4 x 6 x 0.75 cm (Fig. 2.1.6.1). The slabs are mounted in aluminum vanes with a 1 mm separation and are cooled using high speed (Mach 0.1) helium cooling gas. This year crystalline boules with diameters of 3.5 and 6.5 cm that can be fabricated into crystalline slabs, were produced. Two full size laser slabs can be fabricated from each large diameter crystal boule. The boules are grown at both LLNL and Northrop-Grumman with the primary goal of improving optical quality, yield, increasing size and ultimately developing a commercial source for Yb:S-FAP.

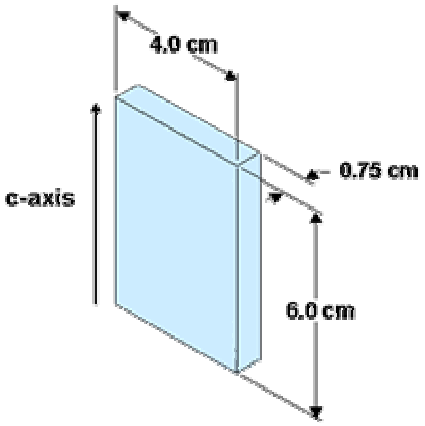

Fig. 2.1.6.1 Yb:S-FAP dimensions required for the Mercury design

Crystals of Yb:S-FAP are grown by using the Czochralski method in three growth stations. A schematic of the furnace design and crystal growth chamber is shown in Fig. 2.1.6.2. The growth station consists of a Czochralski crystal puller, a 50 kW induction power supply, and a computer program that is used for automatic diameter control of the crystal. Automatic diameter control is achieved by weighing the crystal as it is growing and calculating the mass gain per unit time (grams/hour). A 5 x 5 mm or 7 x 7 mm rectangular seed cut along the growth direction is used to initiate the crystal growth process. Growth involves achieving the correct melt temperature, growing an extension to the seed crystal, then ramping the diameter from the initial diameter to the final diameter (either 3.5 or 6.5 cm). Once the correct outside diameter is achieved, this diameter is kept constant at the given pull rate. In order to carefully regulate the growth process, chillers have been added to control cooling water temperatures to the power supplies and the heat load, and a motor generator was installed to dampen line power fluctuations to the crystal growth power supplies. Most recently three new power supplies were purchased to increase the power stability and reliability during crystal growth and will be installed next year. An iridium crucible was chosen to contain the melt. Iridium does not chemically react with Yb:S-FAP and has a high melting temperature. Zirconia is the main insulation component in the furnace as shown in Fig. 2.1.6.2. The iridium crucible and melt therein are heated by inductive coupling of the crucible and copper induction coil. Due to thermal stresses, approximately 3 growth runs can be obtained before the ZrO_2 tube requires replacement.

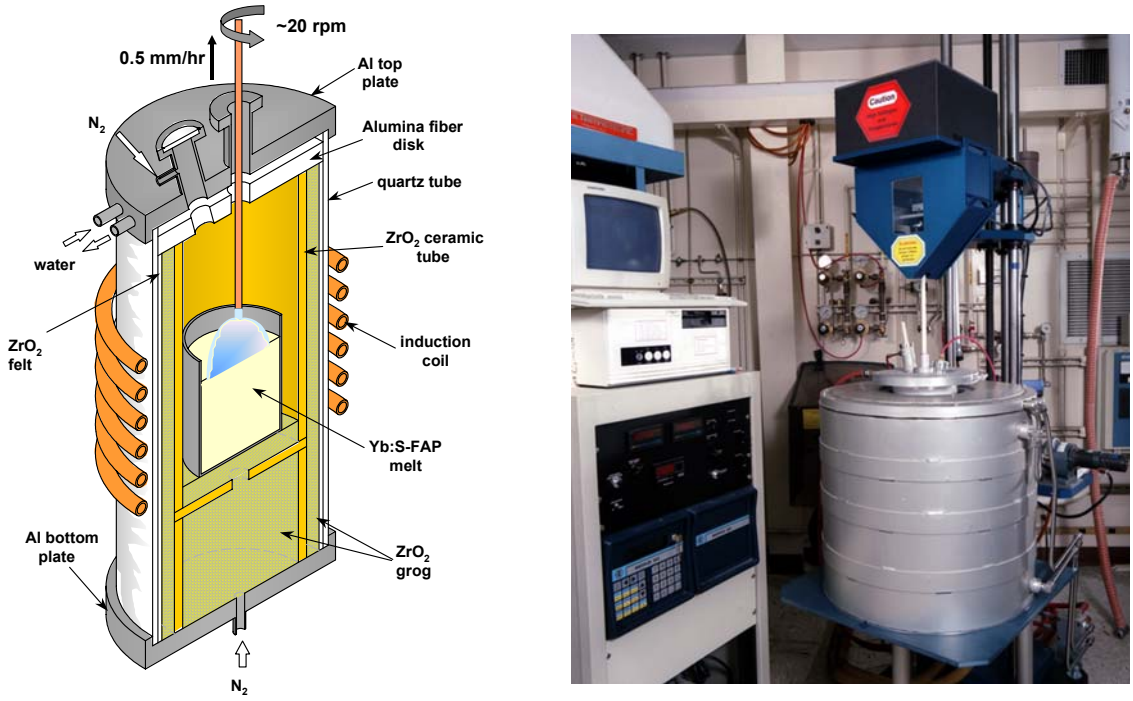

Fig. 2.1.6.2. Schematic of the furnace design with approximate growth parameters and picture of the Czochralski crystal growth station used for Yb:S-FAP growth.

The time required to grow Yb:S-FAP crystalline boules of suitable size to harvest slabs is approximately 17-25 days. A pull rate of 0.5 mm/hr and rotation rate of 15 rpm are used to minimize defects and provide a stable convex melt-interface that does not introduce unwanted fluctuations that can perturb the growth. One of LLNL's three furnaces has been reconfigured to increase the boule diameter. This will allow a yield of two slabs per boule without the need for time intensive, high temperature bonding. The approximate location of both slabs relative to a typical large diameter boule is shown in Fig. 2.1.6.3.

In FY2004, upgrades to the power supplies have been made to provide additional stability and the third furnace was converted to a large diameter growth station. The large diameter furnace was successfully installed and shows promise for providing high quality, 6.5 cm diameter Yb:S-FAP crystals. In addition, a LabView computer program was written to replace out-of-date control systems and add capability for in-situ changes in rotation rate and pull rate. The diagnostics have been upgraded to monitor all aspects of growth, and allows for improved analysis of crystal growth results. In a parallel effort, we have continued a commercial contract with Northrop Grumman to grow 6.5 cm diameter crystals. These crystals produce full size slabs that do not require the separate step of diffusion bonding. Growth efforts have been successful in producing ten large diameter crystals from which six full size non-bonded slabs were harvested for the Mercury Laser. Grain boundaries remain an important issue concerning large diameter crystal growth. Growth parameters are being modified in the upcoming year to eliminate or dramatically reduce grain boundaries and provide higher quality slabs. There are eight slabs in the Mercury laser, with twenty more slabs (bonded and non-bonded) in various steps of fabrication.

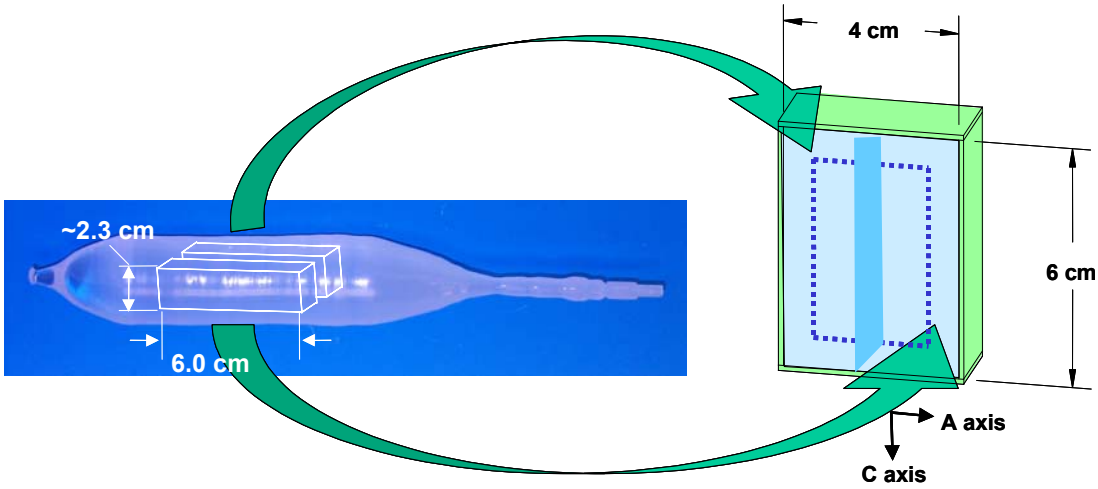

Fig. 2.1.6.3 Current growth geometry of a Yb:S-FAP boule depicting the orientation of slabs for diffusion bonding.

Once the crystal is grown, there are several fabrication steps required to create a full sized slab from either a small boule or a large diameter boule. The crystals are first cut and polished for inspection of defects and suitability for slabs. Then the crystals are water-jet cut with a specialized instrument featuring a particularly thin, high-pressure, stream of water. The cut sections are shaped into half-sized slabs for the bonding process or directly into full size slabs (for the larger boules). Each of these steps and the progress of each step are shown in Fig. 2.1.6.4 for small and large diameter crystals. We have continued to work with an outside vendor to successfully cut small and large diameter crystals by the water jet method.

We are working to develop two bonding processes for Yb:S-FAP crystals to piece together smaller crystals, yielding full size slabs. First, we have contracted with a company to bond the half-size slabs of Yb:S-FAP crystals together as shown in Fig. 2.1.6.5. Scratches and particulates have been a continuing problem in inhibiting the ability to diffusion bond Yb:S-FAP without incurring large phase distortions near the bond line. Process control issues still plague the ability to produce a defect free bond in Yb:S-FAP by this bonding technique.

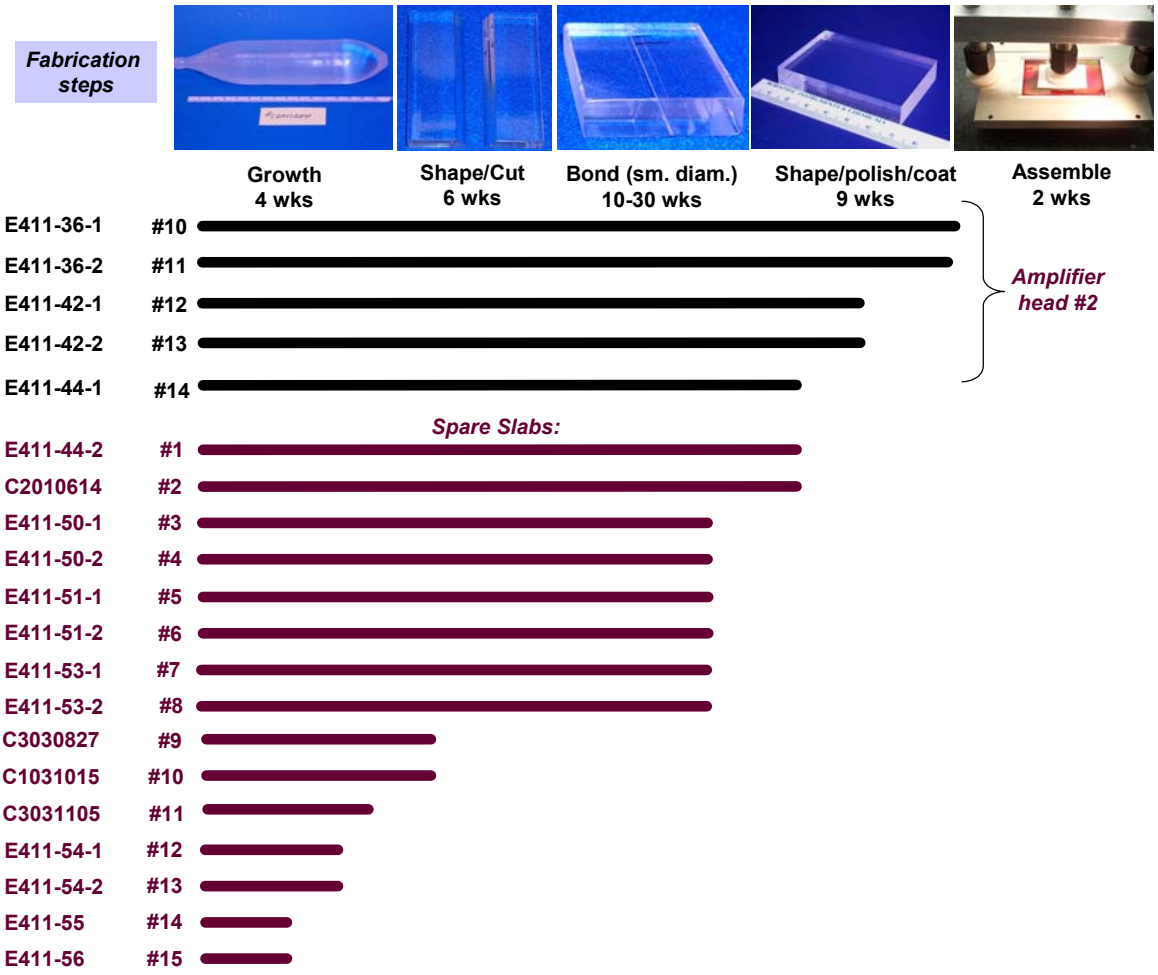

Fig. 2.1.6.4 Fabrication steps and progress tracking in fabricating the crystalline slabs for Mercury.

We are continuing a contract with a second commercial vendor exploring an alternate technique that relies on a low-temperature solution for bonding of Yb:S-FAP. The new process relies upon a method currently utilized for bonding silicate and phosphate-based glasses. In this technique a chemical solution is placed between two polished crystals where it reacts with the surface and cures (i.e. evaporates), forming a bond between the two surfaces. Features to solution bonding are a reduced surface flatness specification ($\lambda/3$), and reduced roughness requirement (approximately 250 Å) compared to the previous process. Our first attempts at solution bonding have been very encouraging. We have produced clear optical bonds although a few bubbles are still present. An example is shown in Fig. 2.1.6.5. Damage threshold measurements have shown initiation of damage at laser fluences greater than 30 J/cm^2. In the past year, we have identified a new process which has repeatedly produced clear bonds with no bubbles. These bonds have passed tests for machinability, reflectivity, damage threshold, heating, and clarity.

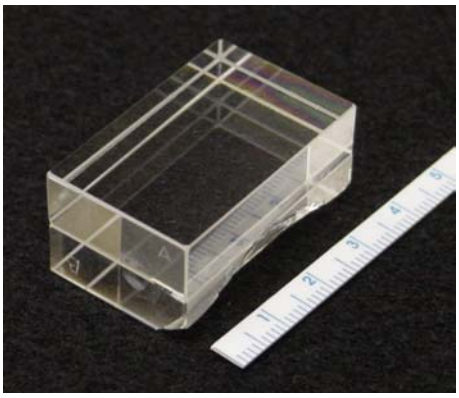

Fig. 2.1.6.5 Solution bonded pair of Yb:S-FAP crystals.

Magneto-rheological finishing (MRF) is used to remove sub-surface damage in Yb:S-FAP slabs and to yield extremely flat surfaces with less than 1 nm roughness [2]. The process for MRF polishing was transferred from LLNL to a commercial vendor. MRF differs from conventional polishing techniques in that a magnetic polishing slurry is forced over the surface of the Yb:S-FAP crystal in a sheering motion by a magnetic ribbon. MRF is a well-known technique for removing imperfections in the transmitted wavefront of a slab by imprinting the inverse wavefront on one surface of the slab. MRF has removed the large stress induced distortions created by the diffusion bonding process, (when two half slabs are brought together to make a full size slab) in addition to removing distortions around grain boundaries to improve the transmitted wavefront. Currently, ten slabs have been wavefront-corrected by MRF and seven additional slabs (four bonded and two full-size) are awaiting MRF. Results of the MRF process are illustrated in Fig. 2.1.6.6.

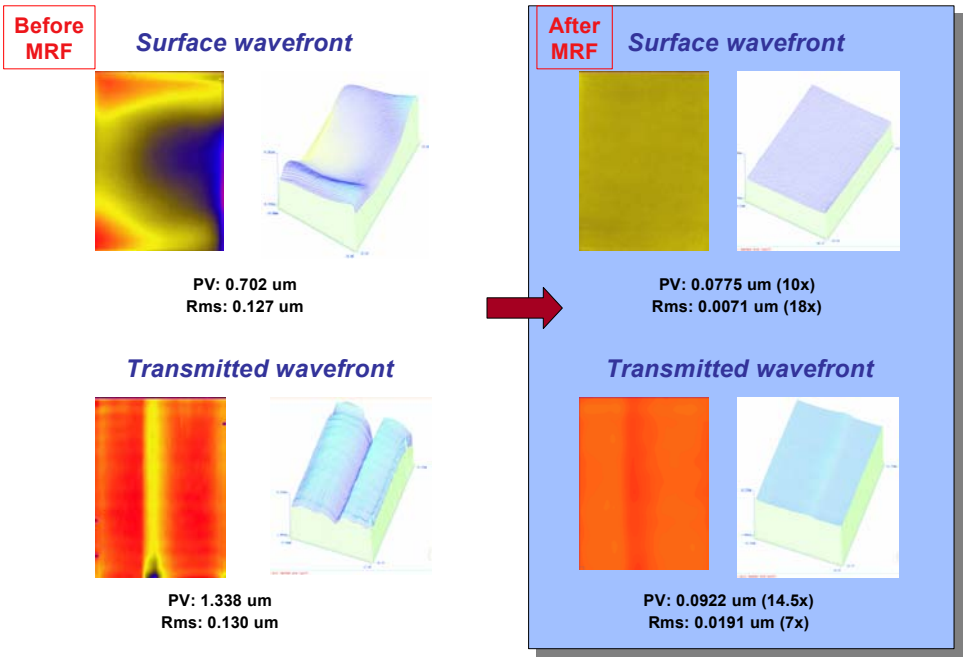

Fig. 2.1.6.6 Before and after results of MRF on surface flatness of Yb:S-FAP slabs and removal of distortions in the transmitted wavefront by the bonding process.

We have continued our efforts in large diameter Czochralski crystal growth to produce larger diameter crystals for full size slabs and future systems. Northrop has grown ten 6.5 cm diameter boules (Seven are shown in Fig. 2.1.6.7.) that have yielded six full-size slabs. We are very encouraged with the growths to date. Defects yet to be mitigated include low angle grain boundaries and cracking of the boule near the bottom. Grain boundaries are the largest concern as they create phase distortions in the slabs, as shown in Fig. 2.1.6.8. The bubble core has been reduced to an approximate 2 cm central region, which is small enough to harvest slabs from around the outside. In the last year, Northrop has also been working to fine-tune their furnace design, boule shape, and growth parameters to reduce defects and produce higher quality, larger diameter crystals. We are now working toward the full elimination of grain boundaries and to develop a reproducible growth method that will control the defects and minimize fracturing from grown-in stress. This will make it possible to fabricate up to two full size parts from each crystal.

Fig. 2.1.6.7 Seven of the ten, 6.5 cm diameter Yb:S-FAP crystals grown at Northrop Grumman.

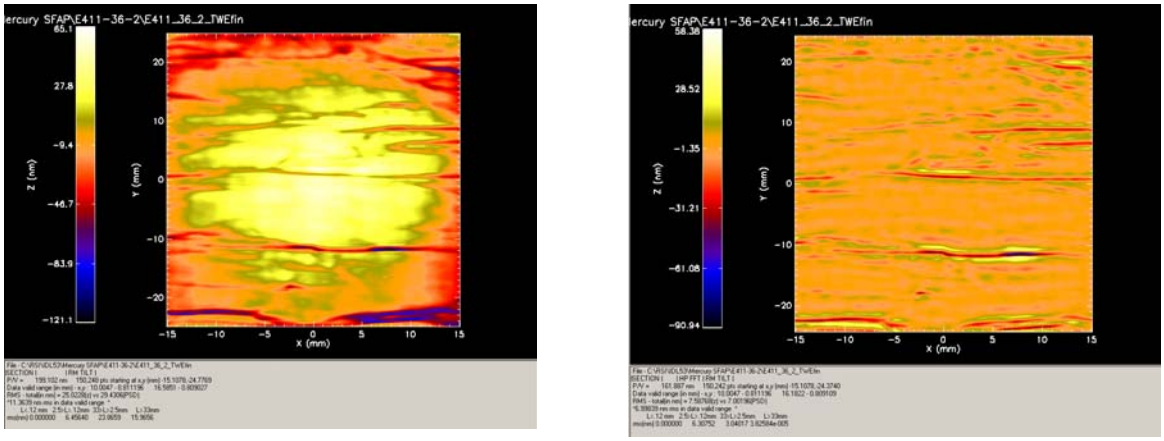

Fig. 2.1.6.8 Before (left) and after (right) results of MRF on transmitted wavefront of Yb:S-FAP slabs. Note removal of distortions resulting from surrounding grain boundaries. Figure on right has been filtered with a 3 mm aperture to simulate pinhole transmission.

In summary, a reproducible growth process for high optical quality 3.5 cm diameter Yb:S-FAP crystals has been achieved. Growth stations at LLNL have been upgraded with more stable power supplies and one furnace was retrofitted with the capability for 6.5 cm diameter growth. In addition, significant progress has been made in growing greater than 6.5 cm diameter crystals of Yb:S-FAP; ten boules were grown yielding six full size (non-bonded) slabs with the potential for ten additional slabs upon further fabrication. Grain boundaries are the remaining defect to be eliminated in the upcoming crystal growths. There are currently 10 slabs in the Mercury amplifier, with 18 additional slabs in fabrication.

[1] K. I. Schaffers, J. B. Tassano, A. J. Bayramian, and R. C. Morris, "Review of the Growth of Yb:S-FAP Crystals for the Mercury Laser" J. Crystal Growth, **253** p. 297 (2003). [2] Cheng, Finnie, Vardar, Journal of Engineering Materials and Technology, **114** p. 137 (1992).

2.1.7 Facility Upgrade

The primary goal was to activate the laser system with two amplifier heads under extended operations. Experiments in the upgraded facility began with four S-FAP slabs installed in a single amplifier. The system was first operated at the 8 J level at 10 Hz for $5x10^4$ shots, then ramped to the maximum diode pump energy, producing 12 J output at 10 Hz for approximately $1.2x10^4$ shots before the system was intentionally turned off. During operations, the new backplane diagnostic cameras were used to verify the absence of parasitic beams or observable backplane power changes (see Fig. 2.1.7.1). After operations, the diode arrays were subjected to a new diagnostic called the "10 amp test". An automated LabView program successively measured the voltage on each diode tile on the array when the current was set at 10 amps. The voltages were then compared to reference values when the diode arrays were assembled.

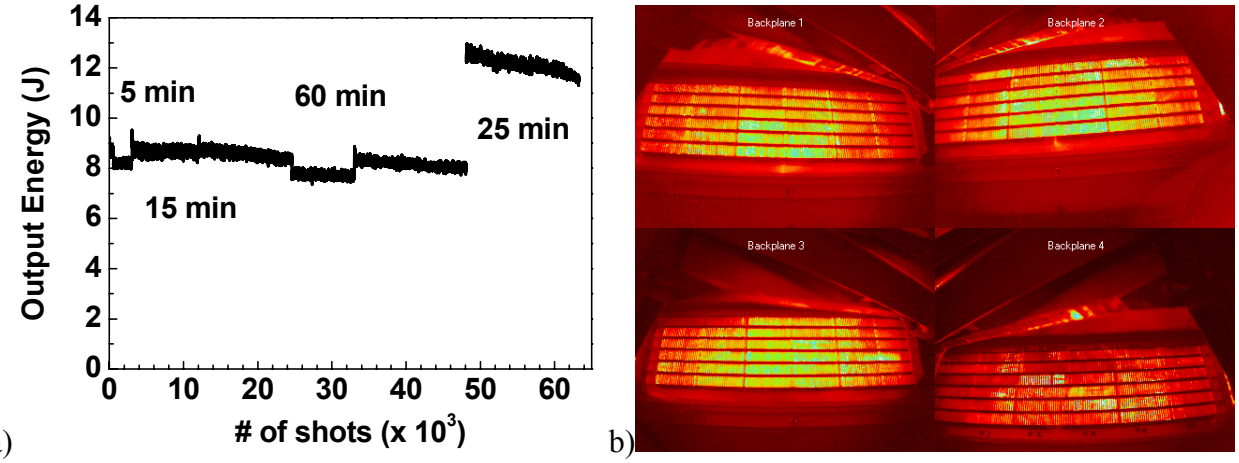

a) b)

Fig. 2.1.7.1 a) 4 slab system operation showing long term operation without damage, b) backplane diagnostic camera screen shot showing diode arrays firing.

Thermal wavefront measurements reveal a stable phase distortion (see Fig 2.1.7.2). Since the thermal model does yet not take into account heating of optics the model differs from the experimental data. Active cooling of the pump delivery system is one of the facility upgrades which will be tested in the coming months to better understand these differences.

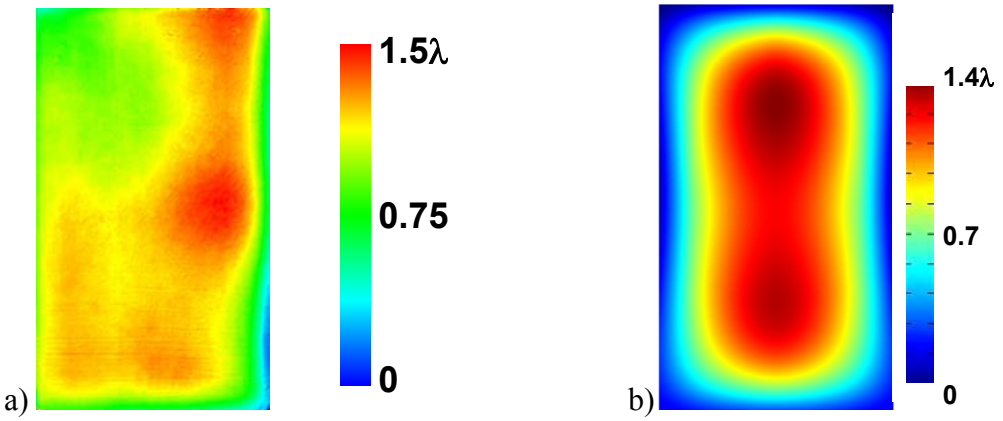

Fig. 2.1.7.2 a) Thermal wavefront of the 4 slab amplifier pumped at 900 ms and 10 Hz, b) model of thermal distortion of the seven S-FAP amplifiers.

Following the thermal wavefront measurements, the several amplifier elements or vanes were stored while the second amplifier systems were being activated. When the vanes were removed from storage, corrosion was observed on two of the vanes. Further investigation revealed that both the aluminum alloy (7075) of the vane material and the coolant chemistry required changes to avoid corrosion. Therefore, new vanes were fabricated from aluminum alloy 6061 (an alloy resistant to corrosion) and chemical additives were added to the cooling liquid. It was decided to alter the edge cladding to improve the heat transfer. A thinner absorptive Schott glass, KG5, (absorption coefficient approximately 45 cm^{-1}), with a thickness of 320 microns was chosen.

In an effort to maximize our existing capabilities, while new parts were being fabricated, four of the slabs were left in their original vanes with the provision that no water cooling be used, and the repetition rate limited to 3.3 Hz. Four new slabs, which had undergone MRF were potted in new vanes with the thinner cladding. These eight slabs (4 old, 4 new) were enough to activate the two amplifier system under restricted operating conditions.

With this arrangement, the laser system, including the average power Pockels cell, was successfully activated in August 2004. Using an injected front end energy of 35 mJ, the single shot output energy of the system achieved 38 J. Model predictions of the expected output energy included amplified spontaneous emission (ASE) as a variable parameter. The ASE parameter represents a gain loss to the system from parasitic spontaneous emission. Initial fits to the data using theoretical ASE models predicted excessive loss, which resulted in the model predicting a lower output energy than was measured. By fitting the ASE parameter to measured excited state lifetime data, we achieve the model fit shown in Fig. 2.1.7.3 (a). The output pulse shape shown in Fig. 2.1.7.3 (b) is unclipped and shows less than 30% modulation. The far field contains approximately 76% of the energy in a 5 times diffraction limited beam. The temporal profile of the input beam is set by the oscillator which is a free running Q-switched Nd:YLF oscillator tuned to the 1047 nm emission line. The input pulsewidth is approximately 25 ns full width at half maximum, while the output pulse experiences gain narrowing (if the input was a square pulse this would be square pulse distortion) to approximately 20 ns full width at half maximum (Fig. 2.1.7.3 (c)). The system was first run at 1 Hz for several short bursts up to 5 minute operations. These short bursts were then repeated at 3.3 Hz before the system was successfully operated 3 hours or 3.6×10^4 shots without damage (Fig. 2.1.7.3 (d).

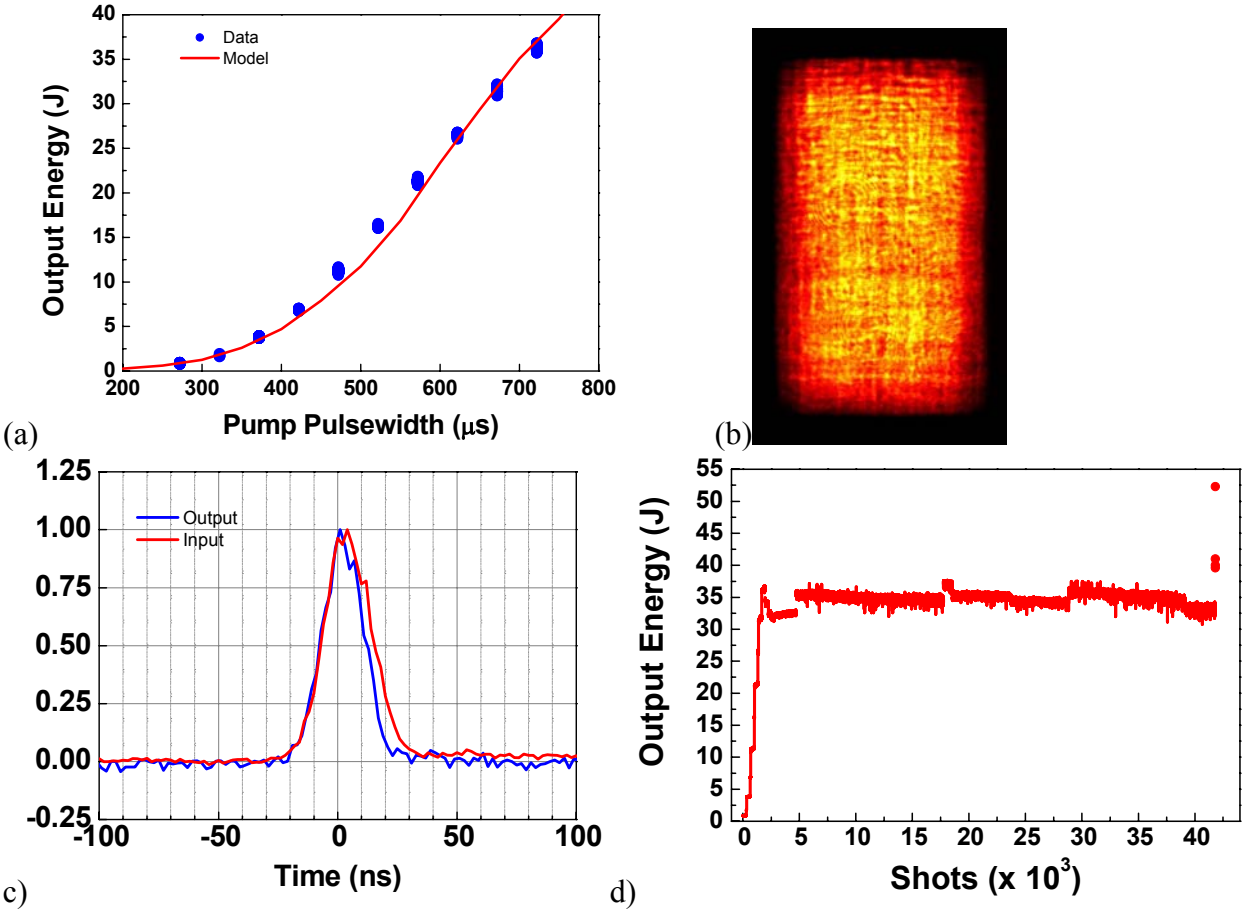

Fig. 2.1.7.3 (a) The output energy gain curve versus diode pump pulsewidth up to 38 J showing overlap with model, (b) nearfield screen shot from the 3.3 Hz operations, (c) Temporal trace of input and output beam showing gain narrowing to 20 ns full width at half maximum at the output, (d) 3.3 Hz operations for 3 hours for a total of 3.6×10^4 shots. The final high energy shots demonstrate capability up to 55 Joules – obtained by increasing the diode pump pulse time.

2.1.8 Advanced Wavefront Control

Mercury will require wavefront correction for the thermally induced distortions within the amplifier. In addition, recent advances in wavefront correction technology might make it possible to also correct additional, higher order wavefront errors due to polishing or bonding in the amplifier slabs. A wavefront correction system is composed of three separate subsystems: a wavefront corrector, a wavefront sensor, and a control system (see Fig. 2.1.8.1). The driving requirement for any wavefront correction system is the spatial frequency of the aberrated wavefront. The specification of an upper spatial frequency limit for the wavefront correction system directly dictates the density of actuators for the wavefront corrector, the resolution of the wavefront sensor, and the complexity and cost for the controls and data reduction algorithms.

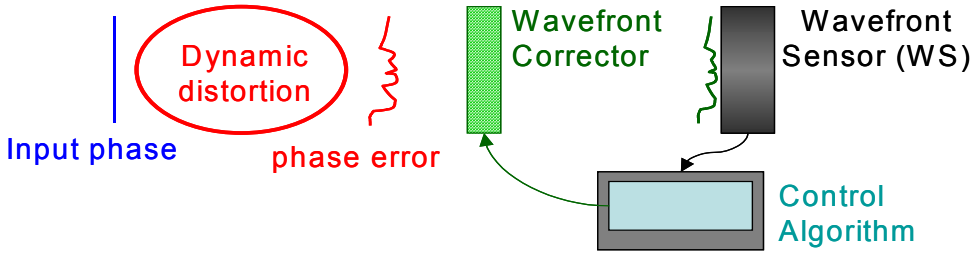

Fig. 2.1.8.1. Schematic of wavefront correction system

The estimated Mercury wavefront distortion can be broken into a 'wavefront budget' as follows:

1. 19 optics at λ/10 each (static)
2. 14 amplifier slabs at λ/5 each (static)
3. Thermal loading on amplifiers approximately 2λ (dynamic)
4. Air currents, thermal loading on lens, etc. approximately 2λ (dynamic)

While phase plates are able to correct static distortions, dynamic distortions require an adaptive wavefront control system. These estimates indicate that a nominal 4 waves of correction is required for an adaptive wavefront control; furthermore, these distortions are nominally low spatial resolutions (see Fig. 2.1.8.2). The high spatial resolution requirement comes from the polishing errors on amplifier slabs. It is unlikely that a single system will be capable of handling both the low and high spatial order wavefront errors and therefore strategy was use a two-tier system with a low spatial order adaptive wavefront control and an advanced high spatial order wavefront correction system.

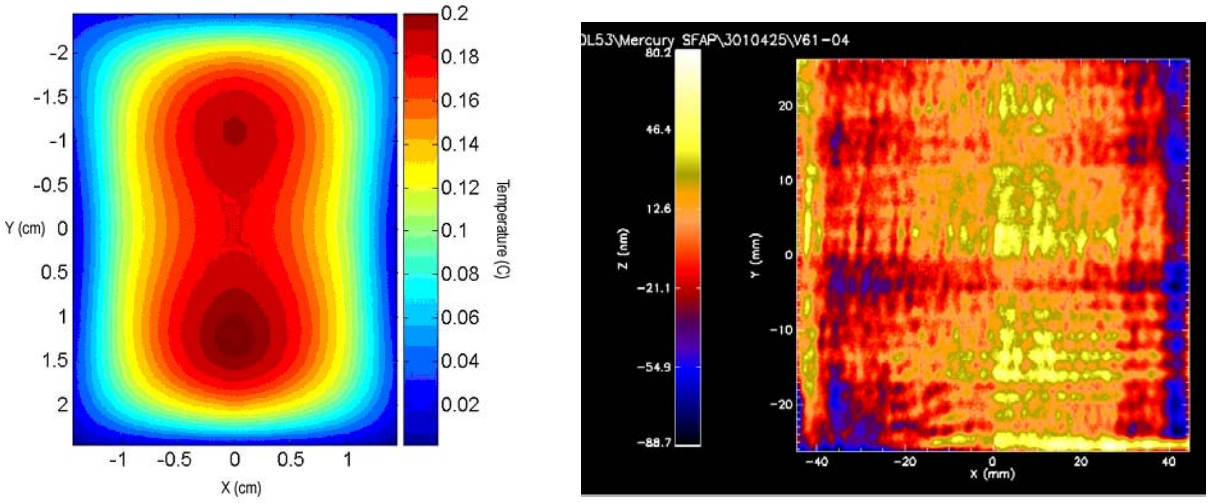

Figure 2.1.8.2. Predicted thermal loading (left) and measured static wavefront (right) on a single amplifier slab.

The specifications for a wavefront sensor and deformable mirror that can correct low spatial order frequencies are listed in Table 2.1.8.3.

Table 2.1.8.3. Specifications for wavefront correction system.

Description	Baseline	Enhanced Performance
Aperture [mm]	45x75	-
Surface Flatness (P-V) [μm]	0.1	-
Surface P-V correction [μm]	4.00	6
Max spatial frequency [1/cm]	0.5	1
Wavelength [nm]	1047	-
Energy [J]	35	-
Pulse width [ns]	3	-
Average Power @ 10 Hz [W]	300	-
Peak Intensity [GW/cm^2]	2.6	-
Fluence [J/cm^2]	1.04	5.19
Resolution [points]	128 x 128	256 x 256
Rep. Rate [Hz]	3	-
Closed loop operation	yes	-
Sensitivity [waves]	0.05	-
Dynamic range [waves]	0.01 -10	-

2.1.9 Front End Laser Upgrade with Spectral Sculpting

The front end laser provides the temporally and spectrally shaped pulse that is injected into the main laser system. The baseline design provides the capability of temporally shaping the pulse in addition to adding and shaping 300 GHz of bandwidth while providing sufficient energy to seed the Mercury Yb:S-FAP amplifiers. A majority of the design is fiber based with only spectral generation, spectral shaping, ASE suppression and final high-energy amplification being done in bulk components. Figure 2.1.9.1 shows a block diagram of the entire system as it is currently designed.

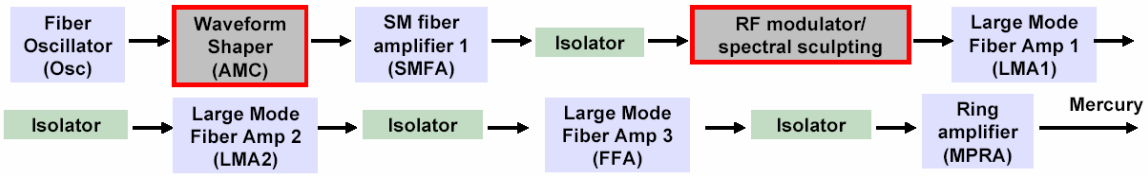

Figure 2.1.9.1 Block diagram of Mercury front end upgrade design.

The design begins with a commercial fiber-based Distributed Feed Back (DFB) tunable oscillator. This oscillator output is fiber-delivered to the Amplitude Modulation Chassis (AMC) consisting of an electro-optic modulator and an arbitrary waveform generator. The AMC provides the capability of temporally shaping the seed pulse to compensate for square pulse

distortion in addition to generating the 960 Hz pulse train used by the remainder of the fiber front end. The temporally shaped pulse is amplified in a commercial fiber amplifier. These components are collectively termed the front-end-source and are all rack-mounted components. The output of the front-end-source is transported to the spectral sculptor that adds and shapes the spectral bandwidth. The laser beam is double-passed through a phase modulator. The phase modulator is a lithium niobate crystal housed in a resonant cavity, driven by a microwave oscillator and amplifier. The spacing of the additional frequency components is dictated by the microwave frequency while the total amount of bandwidth added is proportional to the microwave drive power. The single frequency light from the front-end-source is spectrally broadened by this interaction with the phase modulator. The spectrally broadened laser light is then spatially dispersed by a diffraction grating and brought to the Spatial Light Modulator (SLM). Each individual frequency component added by the phase modulator is mapped on to a separate pixel in the SLM. Each spectral component can be modified in both the amplitude and the phase by varying the voltage applied to individual pixels on the SLM.

The next three components in the front end upgrade are the Large Mode Area (LMA) fiber amplifiers. The design consists of three cascaded 30 dB (gain of 1000) fiber amplifiers. Large mode area fibers were chosen to reduce nonlinear effects caused by a small beam diameter and long length normally associated with fiber amplification. The first two stages use 15 μm core diameter fiber with the final stage utilizing 30 μm core fiber. Each stage is pumped by diode lasers operating at 975 nm that are capable of producing up to four watts of average power. Each stage of amplification is separated by components to provide isolation and suppression of amplified spontaneous emission (ASE).

The output of the LMA fiber amplifiers is sufficient to seed a conventional Yb:S-FAP rod amplifier. The rod amplifier uses a multi-pass ring configuration to enable a range of output energies to match the requirements of the main laser. A Pockels cell is used to trap the seed pulse in the ring until the desired energy is obtained, up to 500 mJ at 10 Hz. The multi-pass Ring Amplifier (MRA) heads are designed with a similar design to amplifiers used on Mercury to leverage existing technology already developed.

Commissioning of the front end source entails producing amplified pulses that may be arbitrarily shaped. In addition to assembling the hardware, a control algorithm for closed-loop temporal shaping was written and tested. An example of the temporal control is shown in Figure 2.1.9.2.

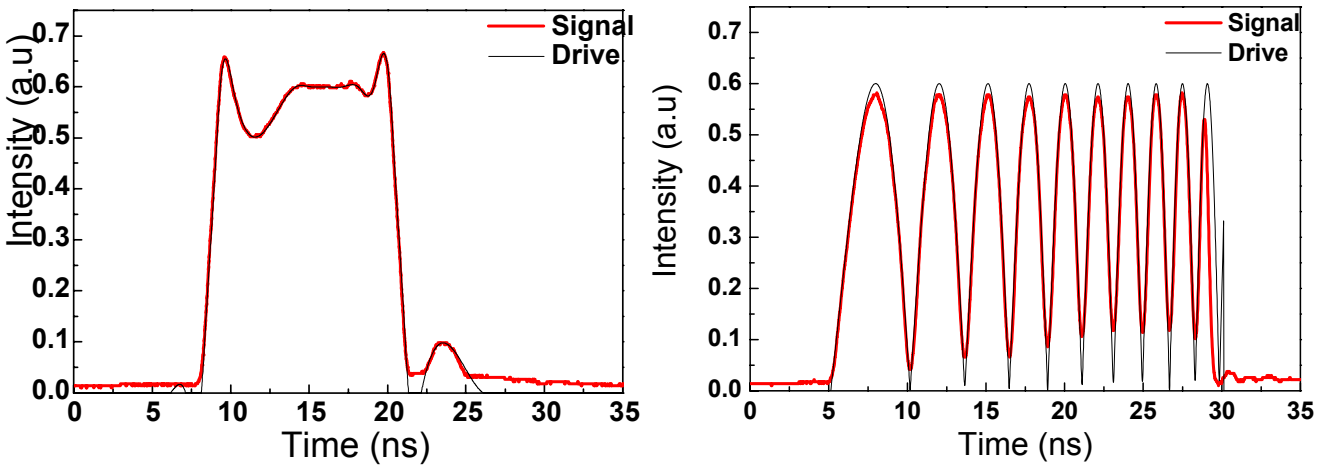

Figure 2.1.9.2 Sample arbitrary amplified waveforms produced by the front end source.

The sculpted waveforms shown in Fig. 2.1.9.2 are not the waveforms to be utilized by Mercury, but demonstrate the ability of the upgraded front end to compensate for square pulse distortion.

Demonstration of the spectral sculptor was completed. The bandwidth generated agreed with theoretical predictions and produced 250 GHz of bandwidth at a drive power of 450 watts. The 250 GHz of bandwidth is easily in excess of the presently envisioned operating point of 150 GHz. Figure 2.1.9.3 shows theoretical predictions of performance and the corresponding spectrum at 450 watts of drive power.

Bandwidth production at various drives

Spectrum generated with 450W drive power

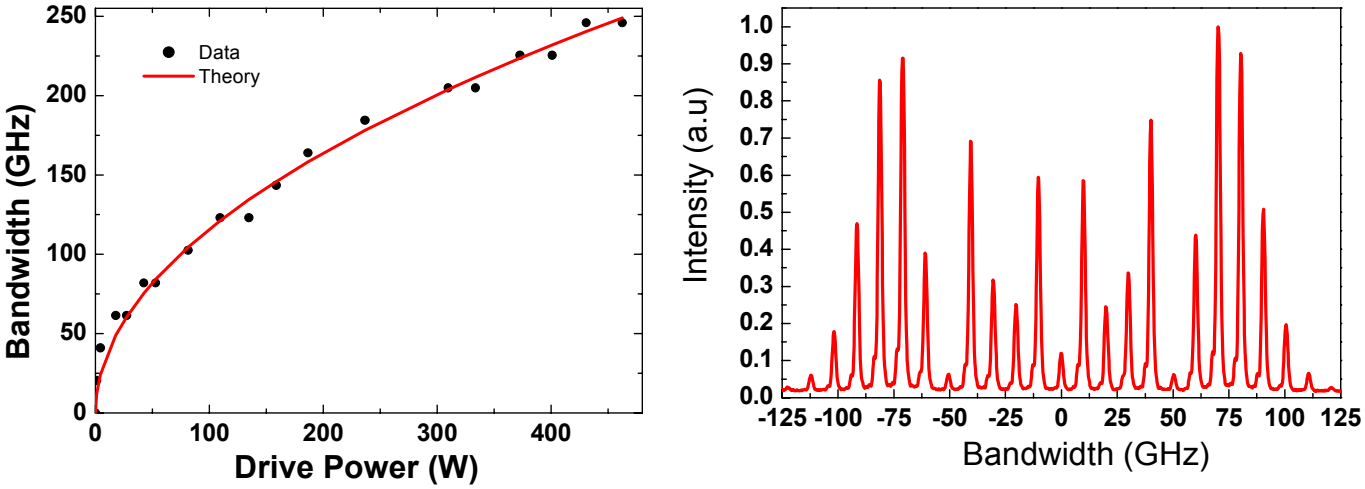

Figure 2.1.9.3 Spectral generation performance (left) and sample spectrum at 450W (right).

In addition to generating the required bandwidth, a basic demonstration of the spectral shaping capabilities was completed. This open-loop shaping demonstration applied a Gaussian transmission mask similar to that which will be required during operations on Mercury. Figure 2.1.9.4 shows the effect of applying a transmission mask to the spectral sculptor.

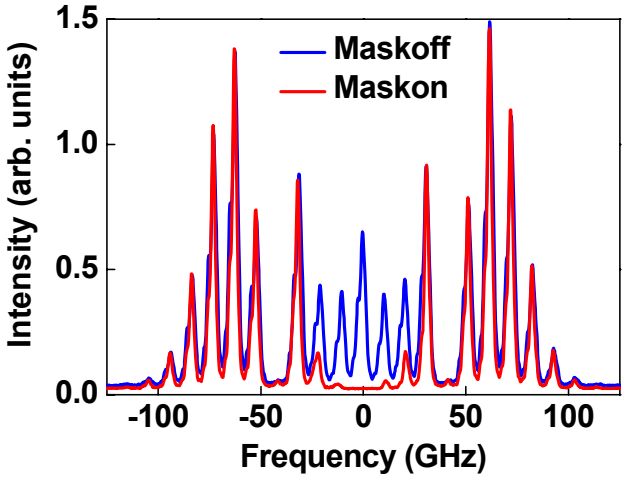

Figure 2.1.9.4 Sculpting demonstration with a Gaussian transmission mask.

Construction of the first stage of the LMA fiber amplifiers was completed in FY2004. The fiber amplifier demonstration consisted of creating 30 dB of gain while maintaining the state of polarization and beam quality of the input. Figure 2.1.9.5 shows the measured gain of the system and the output mode quality of LMA amplifier 1 as a function of the diode drive current. Negative 'gain', as seen in Fig. 2.1.9.5, indicates absorption of the seed light in the fiber. As the diode pump light is increased, the fiber amplifier begins to show (positive) optical gain.

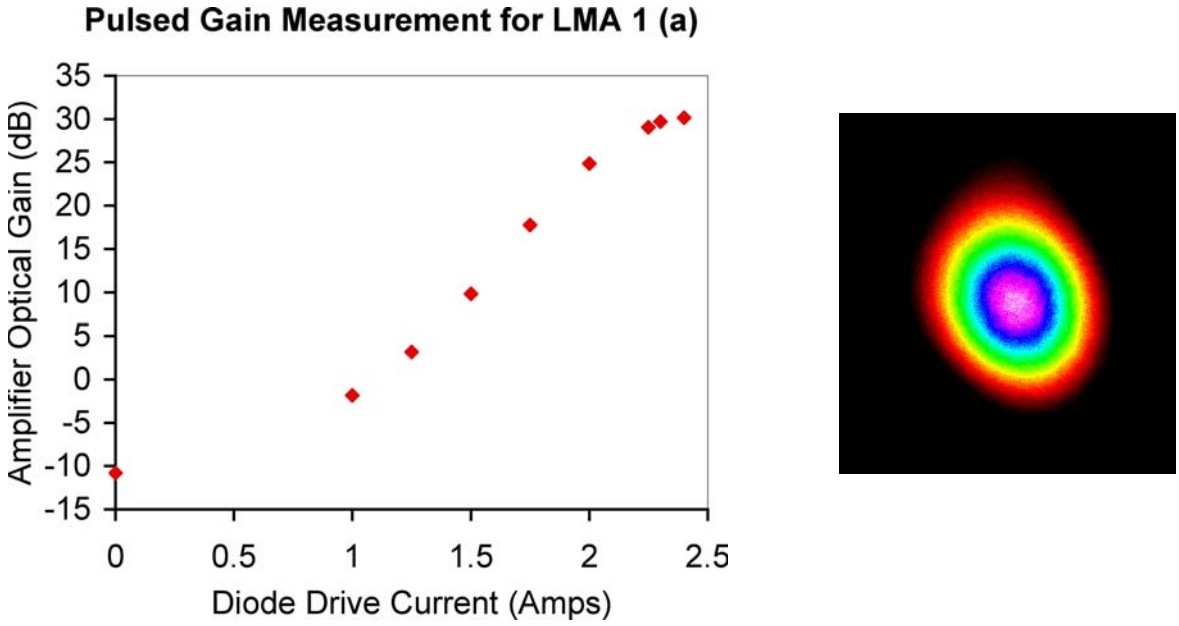

Figure 2.1.9.5 LMA 1 gain measurement (left) and output mode quality (right).

In addition to the above work, the design and procurement of the major components of the ring amplifier heads have been completed. Procurement of the hardware for the final two LMA amplifier stages is also complete. Figure 2.1.9.6 shows the system as built (FY2005).

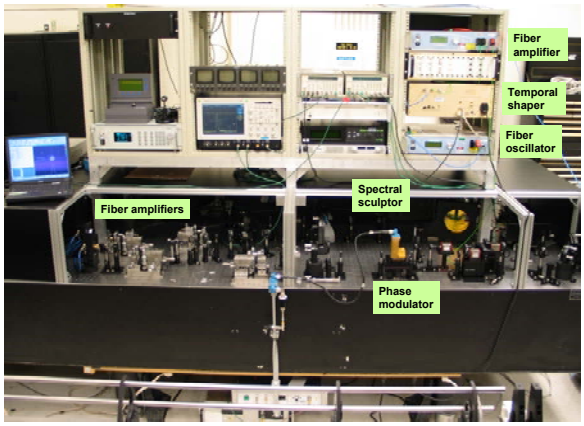

Figure 2.1.9.6 Front End Upgrade system.

2.1.10 IRE Modeling

Modeling studies have continued in which prototype IFE beam line configurations are conceptualized and optimized. As an example shown in Fig. 2.1.10.1, we have conceptualized an IRE beam line using 13 cm x 20 cm Yb:S-FAP slabs doped at $2x10^{19}/cm^3$ Yb^{3+}. This choice of slab size represents a compromise between the contrasting requirements of high efficiency energy storage and high single aperture energy. As aperture size and energy increases, storage efficiency decreases due to depopulation by ASE.

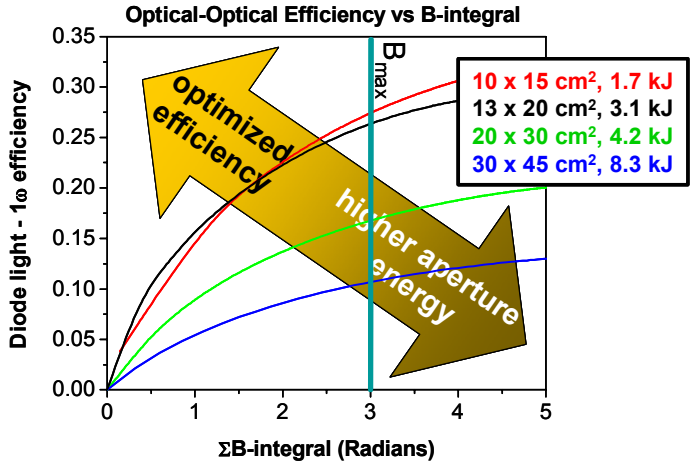

Fig. 2.1.10.1 Yb:S-FAP aperture size is chosen to balance the contrasting requirements of high aperture energy and high energy storage efficiency.

A slab of this size gives rise to output aperture energies of between 3 and 4 kJ at 1ω and leads to plant designs consisting of 1,536 beam lines, corresponding to 16 beams per each port of a 96 port direct drive chamber. Using this approach in which 16 beam lines are bundled and delivered to a single target chamber port, we are also evaluating optimized configurations for constructing shaped drive pulses, such as the picket pulse displayed in Fig. 2.1.10.2, that are both dynamically zoomed and smoothed.

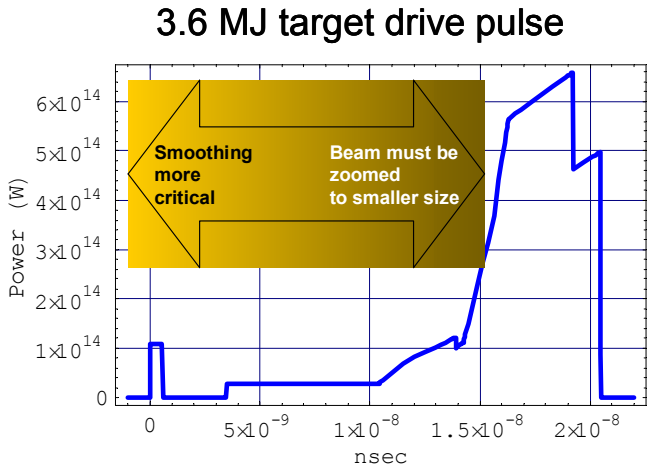

Fig. 2.1.10.2 Picket pulse proposed for direct drive. Target performance can be optimized by dynamically smoothing and zooming the pulse.

Smoothing requirements change during a drive pulse due to the increase in standoff distance (the distance between the critical radius and the ablation front) during an implosion of a direct drive target. Using the rule of thumb that the imprinted spatial frequencies that are of consequence to target stability are those for which,

$$k_{\text{imprint}} \cdot d_{\text{standoff}} < 2 \tag{1}$$

leads to the following plot of maximum l-modes that are of concern at any time during the drive pulse.

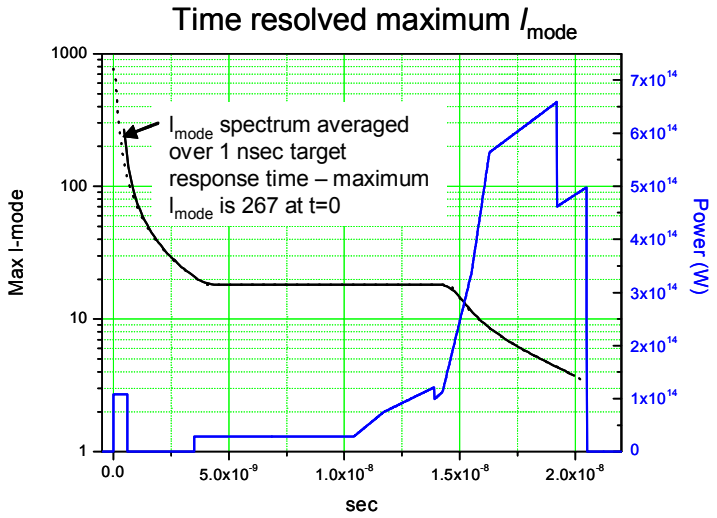

Fig. 2.1.10.3 Maximum l-mode number that contributes to target instability as a function of time into the drive pulse.

For the case of SSD, the maximum l-mode numbers given in Fig. 2.1.10.3 that contribute to target instability can be used to derive a requirement on illumination solid angle for a drive pulse of given bandwidth and desired level of laser imprint on target,

$$\sigma_{tot}^2 = \frac{1}{\left(\Delta\nu \cdot \tau\right)\Delta\Omega_{tot}\left(d_{targ}/\lambda\ell_{\substack{\text{mode}\\\text{max}}}\right)^2\left(\pi/2\right)}. \tag{2}$$

As a specific example we consider a drive beam with a bandwidth of 150 GHz at 1ω and use Eqn. (2) and Fig. 2.1.10.3 data to calculate the required aperture size for a bundle of 16 beams (a single port bundle) at a distance of 20 m from the target chamber center. Because the target is most susceptible to laser imprint and subsequent instabilities early in the pulse, the earlier parts of the drive pulse require more solid angle than the later parts. This naturally leads to the construction of the drive pulse from a superposition of individual pulselets, each pulselet being from a different one of the 16 beam lines that are bundled to a single target chamber port. Not only does this permit the solid angle occupied by the drive pulse to be dynamically changed during the pulse, but it also enables the drive pulse to be dynamically zoomed ensuring

maximum overlap between the drive pulse and an imploding target. This concept is illustrated schematically in Fig. 2.1.10.4.

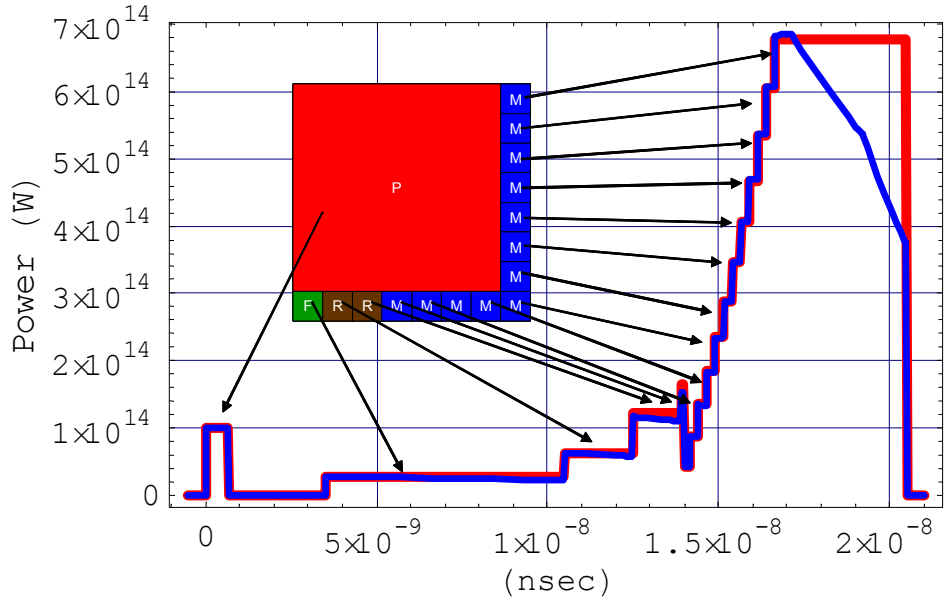

Fig. 2.1.10.4 Schematic diagram showing a picket pulse constructed from 16 individual rectangular in time pulses. The inset shows the allocation of real estate at a given chamber port for the various components that make up the picket pulse. The earliest component, the picket, requires the largest solid angle.

As shown in Fig. 2.1.10.4, the picket drive pulse can be built up through a superposition of the 16 individual pulselets, one from each beam line. Each of these individual pulselets can be rectangular in time, thereby simplifying and improving harmonic conversion. Additionally, because the individual pulselets are spatially separated they can be individually zoomed through the use of a segmented phase plate designed to let the later in time pulselets come to a tighter focus than the earlier ones, thereby dynamically following the imploding target.

2.2 Chambers

2.2.1 Chamber Response and Safety & Environment

Our FY2004 tasks were:

- Complete safety and environmental assessments for the HAPL First Wall Battle plan and blanket design efforts.
- Upgrade chamber codes to account for ion heating.

Safety and environmental assessments were completed for the HAPL First Wall Battle Plan. Specifically, the neutron activation characteristics of pure tungsten and likely tungsten alloys were examined in terms of their radiation damage, waste disposal rating, waste volume, and nuclear afterheat.

For pure tungsten one must replace the wall about every 4-5 years in order to avoid excessive quantities of ^{186m}Re, which can lead to the wall not qualifying for disposal via shallow land burial. This assumes that the first wall would be disposed of as a stand-alone component. Due to its brittleness, it is common to alloy tungsten with rhenium. Unfortunately, this speeds the production of ^{186m}Re, and it fails to qualify for shallow land burial after 2 years of irradiation (assuming an alloy with 3% Re). Figure 2.2.1.1 is a plot of the waste disposal rating (WDR) for pure and alloyed tungsten as a function of irradiation time. For a component to qualify for shallow land burial, the WDR must fall below unity.

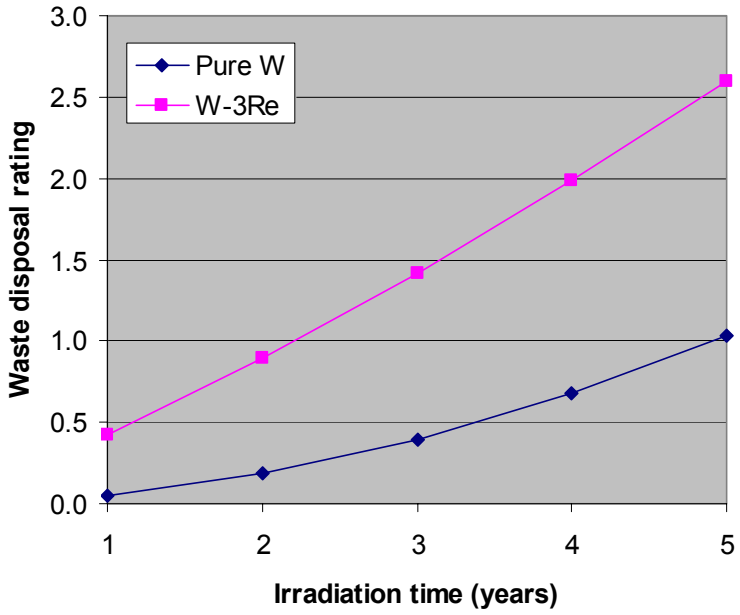

Fig. 2.2.1.1 The waste disposal rating as a function of the irradiation time shows that pure tungsten would qualify for shallow land burial for nearly 5 years, while W-3Re would qualify for just over 2 years.

The helium production and nuclear afterheat experienced in the first wall are inconsequential. The helium coming from the target burn products far outpaces that from nuclear transmutation. The nuclear afterheat is often cited as a concern in the MFE community, but this

is for large components that are primarily made from tungsten. The HAPL first wall contains a relatively thin coating (approximately 100 μm) of tungsten. While this produces a large specific power from neutron activation, the total decay heat is less than 1 MW, and thus, is unimportant.

Our work on safety and environmental issues for the HAPL First Wall Battle Plan is documented in a section of Dr. John Sethian's overview paper [1].

Rather than modify the existing ABLATOR code such that it could account for heating by ions, we opted to develop a new code to model chamber and optic heating and stresses. ABLATOR's use of an explicit numerical method made it slow and difficult to use due to severe timestep/stability constraints. The new code, RadHeat, uses a fast, implicit numerical method and easy-to-read data tables and input files. Although it is a one-dimensional code, RadHeat can model complicated, multi-component, multi-layer materials of highly variable thicknesses and properties. Corrections for grazing irradiation (not perpendicular to the surface) are available. RadHeat calculates heating and cooling by conduction with boundary conditions that allow for convection and radiation. Photons, ions and neutrons can be modeled, and multi-shot calculations are commonplace. Radiation sources can be staggered in time, so relatively complex scenarios can be modeled rather easily.

Figure 2.2.1.2 shows the results for an example RadHeat calculation. It is plot of the time-temperature history of an IFE final optic. The details of the optic heating simulation are as follows:

- target yield = 350 MJ (Perkins' 154 MJ output spectra scaled linearly to 350 MJ)
- chamber / beamtube conditions = vacuum
- optic stand-off distance = 26 m
- optic grazing angle = 85 degrees
- laser fluence = 5 J/cm^2 (normal to the beam)
- laser pulse length = 5 ns (corresponds to peak power of the laser pulse)
- laser reflectivity = 99%
- repetition rate = 10 Hz

Due to the logarithmic scale used for time, it is possible to see the details from the first laser pulse, while only the peaks can be seen for pulses #2-10. In the first pulse, the laser heating of the optic occurs at roughly 10^{-7} s. The next spike is due to heating from the prompt x-rays, which account for 1.4% of the target output. The third and fourth spikes are from the burn and debris ions, respectively. As can be seen, the dominant threat in terms of temperature of the optical surface (and the resulting stress) is the initial laser pulse. Note that the heat transfer coefficient at the back surface (assumed to be 100 W/m^2-K) is inadequate to maintain the starting temperature. One observes the temperature "ratcheting" up with each pulse. Equilibrium is reached in several hundred pulses.

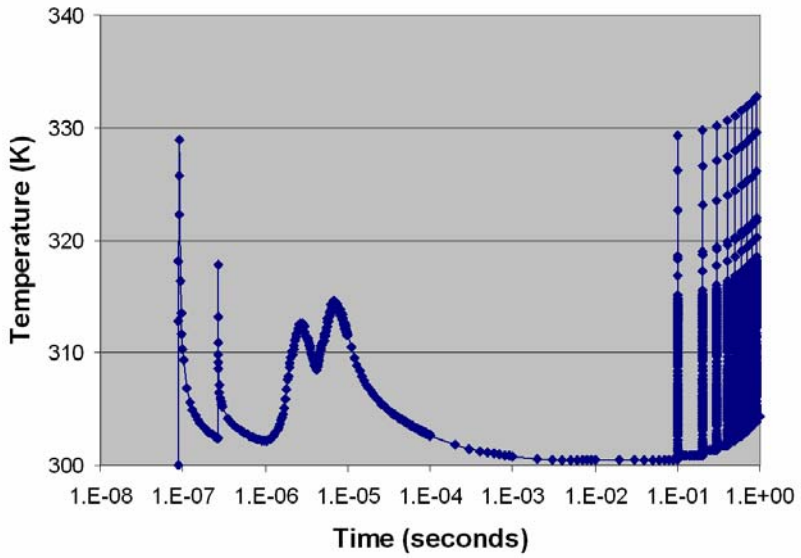

Fig. 2.2.1.2 A RadHeat result for the heating of a grazing incidence aluminum final optic shows multiple features resulting from the first pulse

RadHeat calculations typically require tens of minutes to complete, even for hundreds of pulses. This compares favorably with ABLATOR run times that were many minutes to hours and often suffered from instabilities that would result in a code crash after a significant amount of computing time. Additional information about the RadHeat code can be found in "Effect of Multi-Shot X-Ray Exposures in IFE Armor Materials," which will be published in an upcoming article of the *Journal of Nuclear Materials* [2]. Also, an LLNL report, "RadHeat V1 User's Manual," UCRL-SM-208820 [3] is available.

References

[1] J. Sethian et. al., “An overview of the development of the first wall and other principal components of a laser fusion power plant”, J. Nuclear Materials, 347, p. 1612-177 (2005).
[2] J. Latkowski, R. Abbott, R. Schmitt, B. Bell, „Effect of Multi-shot X-ray exposures in IFE armor materials“ J. Nuclear Materials, 347, p. 255-254 (2005)
[3] R. Abbott UCRL-SM-208820

2.2.2 Radiation Damage Modeling for Chamber Materials

During FY2004, we have made progress in performing numerical calculations for predicting and verifying the thermal conductivity of BCC tungsten as a function of defect concentration. In metals, there are two contributors to thermal conductivity: the phonon and the electron contribution, λ_p and λ_e, respectively. Increases in thermal resistivity, or the inverse of thermal conductivity, is attributed to increases in the density of lattice imperfections, due to the increasing number of collisions encountered by electrons and phonons and subsequent reduction in their mean free paths. Furthermore, increasing thermal energy (temperature) also has the effect of increasing resistivity due to the increased displacement amplitudes of lattice atoms about perfect equilibrium positions.

In this work, classical molecular dynamics and the Green-Kubo formalism [1,2] was used for calculating the thermal conductivity, the main transport property of interest for understanding the effects of radiation damage and damage debris on the performance of the first wall tungsten armor in an inertial fusion energy chamber. To date, we have studied the effect of vacancy point defects. In this work, classical MD and the Green-Kubo formalism is only applicable to modeling λ_p. For pure metals, λ_e is usually the dominant contributor to thermal conductivity, particularly at elevated temperatures. However, it is the reduction of mean free path of electrons due to the presence of such defects as impurities and vacancies that may make the two contributions comparable. In order to calculate the electronic component to thermal conductivity we use the Wiedemann-Franz relations [3-5],

$$\lambda_e = L\ T\ \sigma$$

which relates the electrical conductivity σ with the electronic component of the thermal conductivity λ_e in pure metals, and L and T are the Lorentz factor and the absolute temperatures, respectively. Figure 2.2.2.1 shows λ_p, λ_e and the total thermal conductivity in units of W/m-K as a function of temperature. The total thermal conductivity is taken from experimental measurements in tungsten [6], while λ_e is calculated using the above Wiedemann-Franz relationship, taking electrical conductivity also from experimental measurements [6], and the Lorentz factor as 3.04×10^8 W-ohm/K^2 [3] and assuming it to be constant over all temperature ranges. λ_p is simply taken as the difference between the total measured quantity and the electronic component. We see from Fig. 2.2.2.1 that at 300 K, both λ_p and λ_e are about the same in magnitude, and that λ_p is a significant contributor to the total thermal conductivity at low temperatures to warrant using these expensive numerical techniques.

We performed a 20 ns molecular dynamics simulation consisting of 2000 tungsten atoms in a perfect BCC configuration equilibrated at 300 K. We use the potentials of Krasko for tungsten [7], in the EAM (embedded atom method) formalism. The time step used was 1 fs. We used an ensemble of atoms with a natural isotopic distribution with 5 isotopes, and whose number fractions for the 179.95, 181.95, 182.95, 183.95 and 185.95 amu isotopes are 0.12, 26.50, 14.31, 30.64 and 28.43, respectively. Our calculated λ_p is 160 W/m-K, which compares with 73 W/m-K from Fig. 2.2.2.1. We believe that much of the uncertainty is due to small simulation cell effects and sensitivity of these calculations to the interatomic potentials.

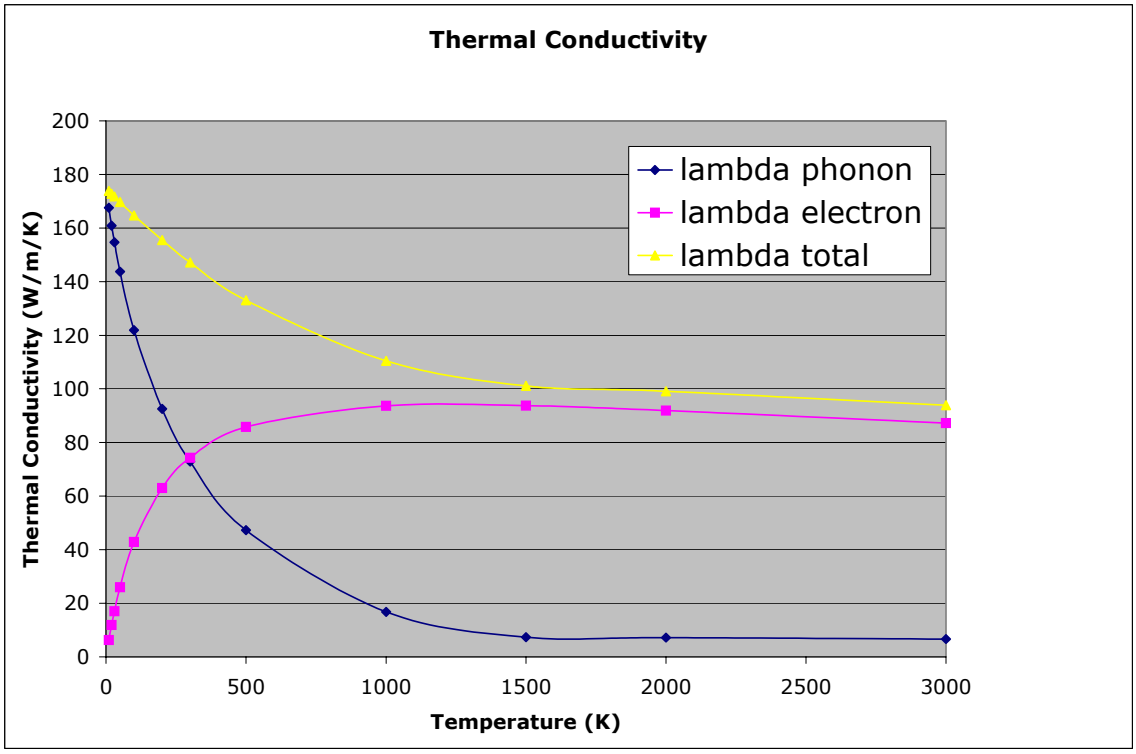

Fig. 2.2.2.1 Total, phonon and electron components of the thermal conductivity for Tungsten at different temperatures.

In addition, we performed a number of simulations to examine the effect of vacancy defect concentration on thermal conductivity. Although it may not be possible to calculate absolute accurate transport properties for tungsten (W) using molecular dynamics simulations, we believe that the scaling behavior with defect concentration may be valid and useful.

Table 2.2.2.1 details the results of simulations to calculate λ_p with varying vacancy point defect concentrations n_v and at different temperatures. We note that λ_p for the pure zero-vacancy simulations produce values twice those inferred by Fig. 2.2.2.1.

Table 2.2.2.1 Results for λ_p for range of temperatures and defect concentrations.

T (K)	n_v	λ_p(W/m-K)
100	0.00	230
100	0.01	29
100	0.02	19
100	0.03	19
100	0.04	18
300	0.00	160
300	0.01	46
300	0.02	26
300	0.03	21
300	0.04	18
500	0.00	112
500	0.01	38
500	0.02	25
500	0.03	21
500	0.04	20

For the three temperatures, we fit λ_p to a power-law form,

$$\frac{\lambda_p^{defects}}{\lambda_p^{pure}} \propto n_{vacancies}^{-\alpha}$$

where α is the power law fitting parameter. For 100, 300 and 500 K, we calculate α to be 0.34, 0.70 and 0.49, and r^2=0.84, 0.99 and 0.97, respectively. Figure 2.2.2.2 below plots of the fit in each case with the power-law model. Although we do not see a clear progression of α with temperature, we note that the 100 K calculations do not produce the best fitting parameters.

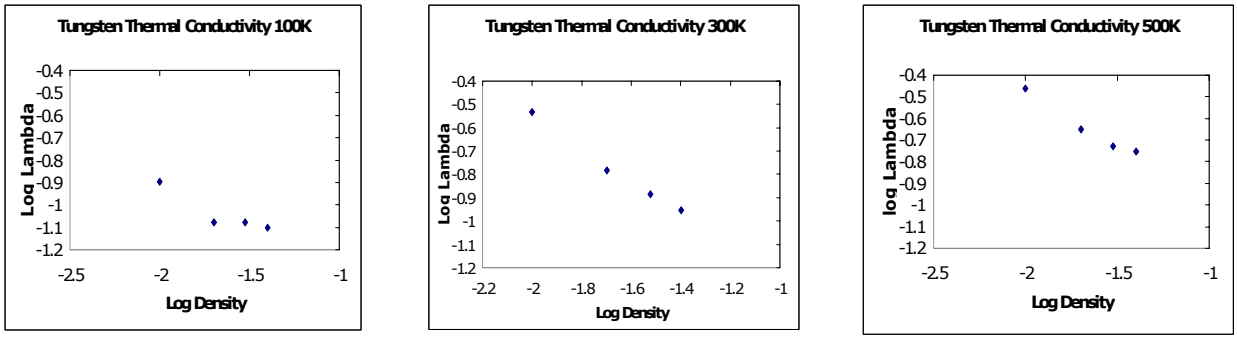

Fig. 2.2.2.2 Thermal conductivity at three temperatures versus the vacancy number density. Plotted are the log λ_p versus log n_v showing good agreement with the power-law model for the effect of defect density on thermal conductivity.

Only limited experimental data that exist to validate these calculations on the effect of point defects on λ_p. In general, there are experiments to measure total thermal conductivity and

the electrical resistivity as a function of radiation dose in dpa (displacements per atom), for which λ_p may be inferred. However, detailed analysis must be performed to determine the point and cluster defect populations present in these experiments in order to make direct comparisons with these simulations.

During this fiscal year, we have chosen not to model the effect of self-interstitial point defects on thermal conductivity. In general, self-interstitial defects are not observed in irradiated pure Tungsten experiments, due to their very small migration barriers and subsequent high mobility for escape at surfaces, grain boundaries and dislocations. This effect is also observed in our simulations, where over short time-scales, on the order of tens to hundreds of picoseconds, that self-interstitial point defect populations have the tendency to aggregate in our simulations.

References for Section 2.2.2

[1] FY2003 HAPL Progress Report, Section 2.2.3

[2] J.-P. Hansen and I. R. McDonald, *Theory of Simple Liquids*, 2nd ed. (Academic Press, London, 1986).

[3] C. Kittel, "Introduction to Solid State Physics", John Wiley and Sons, New York, 1953.

[4] Y. Terada, Ohkubo, T. Mohri and T. Suzuki, Mater. Sci. Eng. A, 1997, 239-240, 907.

[5] G. K. White, "Intermetallic Compounds, Principles," Vol. 1, eds. J. H. Westbrook and R. L. Fleischer, John Wiley and Sons, Chichester, 1017, 1994)

[6] J. Davis, ITER Materials Properties Handbook, http://www-ferp.ucsd.edu/LIB/PROPS/ITER/ 1997.

[7] G. L. Krasko, *Intl. J. of Refractory Metals & Hard Materials* **12** (1993-1994) 251

2.2.3 Chamber Scaling and Scoping Studies

The long-range goal of this work is to develop an improved, integrated systems modeling capability that includes current understanding of the physics, engineering and costing information for candidate drivers, targets, chambers, and power conversion subsystems. In FY2004, we continued to focus on chambers and power conversion systems. The W-armor-coated, ferritic steel first wall (FW) remains the leading candidate for the chamber design. Models for a liquid lithium (Li) cooled FW and breeding blanket have been included in the systems model. Li enters the chamber and first passes through the first-wall cooling channel since this is the region of highest heat flux (due to the short ranged target emissions). After exiting the FW cooling channel, the coolant then passes through the blanket region to remove the neutron heating. There are several constraints that are self consistently accounted for in the chamber model. These include:

- Maximum W surface temperature due to pulsed heating (2400 ^{o}C)
- Maximum average ferritic steel (FS) temperature (600 °C for low activation FS, 700 °C for oxide dispersion strengthened ferritic steel (ODS FS))
- Maximum FS/Li interface temperature (600 °C).

Depending on the target yield, rep-rate, material choices and material thicknesses, any of these constraints could set the operating point. The objective is to achieve the highest possible coolant temperature coming out of the chamber in order to maximize the thermal-to-electric conversion efficiency.

To date, we have coupled this Li cooled chamber to an advanced Brayton cycle for electricity production. The chamber operating conditions and temperature limits determine the total thermal power and coolant inlet and outlet temperatures. These then determine the achievable cycle efficiency. Figure 2.2.3.1 illustrates results from the systems code. Shown are the inner (at the W/FS interface), average, and outer (at the FS/Li interface) temperatures of the FS first wall as a function of the Li coolant inlet temperature. In this case, the 600 °C constraint on the FS/Li interface is the most limiting, restricting the inlet temperature to 475 °C.

Figure 2.2.3.2 shows the Li coolant temperature out of the FW cooling channel and out of the blanket as a function of the inlet temperature. Also shown is the cycle efficiency for these coolant parameters. When the inlet temperature is 475C as determined in Fig. 2.2.3.1, the maximum achievable cycle efficiency is 45%. With low activation FS instead of ODS FS, the inlet temperature is limited to 415 ^{o}C, and the cycle efficiency is 42%.

In FY2005, we will continue development of the systems code. Other coolant/breeder options (e.g., PbLi) and other power conversion cycles (Rankine) will be considered. We will also begin to incorporate costs and cost scaling models for the chamber, balance of plant (i.e., building, heat exchangers, generators, etc.) and the drivers (KrF and DPSSL).

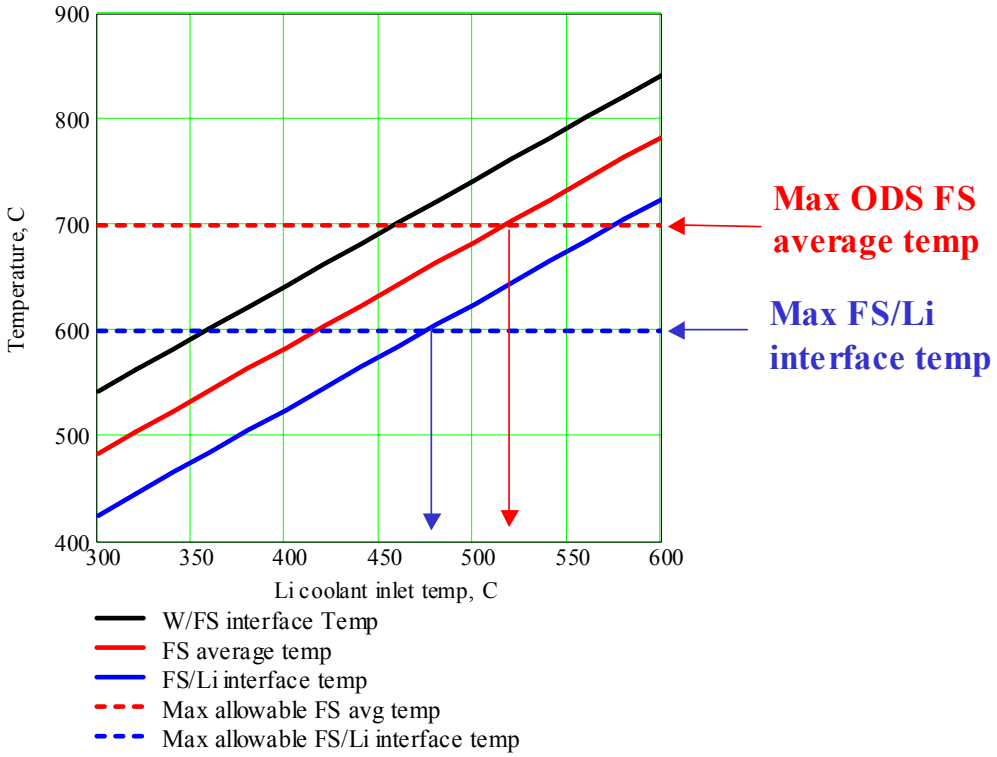

Fig. 2.2.3.1 First wall temperature (inner, average, outer) versus Li coolant inlet temperature. Constraints on average and outer temperature are indicated.

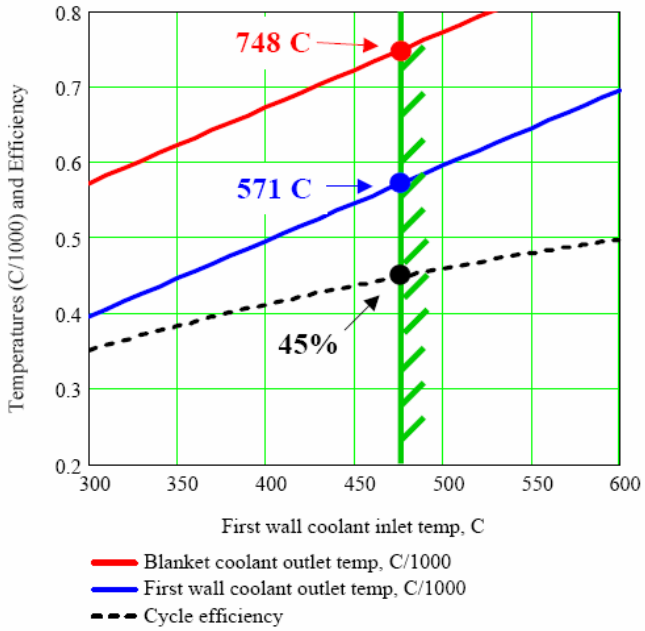

Fig. 2.2.3.2 Coolant temperature out of FW cooling channel (magenta) and out of blanket (red) as a function of inlet temperature. Cycle efficiency (black dashed) is limited to 45% due to constraint on inlet temperature (475 °C.

2.3 Final Optic

2.3.1 Final Optics Irradiation Studies

Our FY2004 tasks were:

- Continue evaluation of optical properties of aluminum and dielectric mirrors under neutron irradiation.
- Conduct alpha implantation experiments and evaluate damage to aluminum mirrors.

The neutron irradiations were conducted at Oak Ridge National Laboratory (ORNL) in the High Flux Irradiation Reactor (HFIR). Ion irradiations were conducted at Lawrence Livermore National Laboratory (LLNL) at the Ion Beam Lab.

Dielectric mirror samples (3ω and 4ω) were originally sent to ORNL during the third quarter of FY2002. The irradiations were completed during third quarter of FY2003, and the first two rounds of samples were returned to LLNL for testing during the first quarter of FY2004. Note that dielectric mirrors are not thought to be a candidate for the final optic. Rather, they are a possible candidate for the penultimate optic, which is not exposed to line-of-sight neutrons. Shortly after receiving the samples, post-irradiation evaluation began for the dielectric mirrors, as these received a neutron dose closest to that expected in the IFE case (due to the lower flux experienced in the location of the penultimate optic).

As we have done in the past, our analysis began with reflectivity measurements using a Shimadzu spectrophotomer. Initially, we noted that our results for these very basic measurements appeared to have significant scatter. Further, they were not repeatable. Testing confirmed that the spectrophotomer was operating properly, and we quickly realized that the samples had significant surface damage. Specifically, the surface was riddled with numerous scratches. The apparent cause of the scratches was the cutting of the samples at ORNL in order to get them to fit into the standard sample irradiation containers. Unfortunately, this surface damage rendered the reflectivity measurements useless. We consulted with several experts, including the head of the Air Force's Optical Characterization and Evaluation Laboratory at Kirkland Air Force Base. Regretfully, everyone agreed that there was nothing that could be done to salvage the desired reflectivity measurements.

In an effort to obtain something useful from the dielectric mirror irradiations, they were sent for evaluation using Cross Sectional Transmission Electron Microscopy (XTEM). Such analyses were performed prior to irradiation as well, so baseline information is available. Results from the XTEM analyses should be available in the second quarter of FY2005.

Dr. Lance Snead of ORNL has offered to repeat the irradiations, while personally shepherding the samples through the process in order to ensure that they are handled appropriately.

Ion irradiation experiments have been completed using an electroplated aluminum mirror provided by Dr. Mark Tillack of the University of California at San Diego. A mirror was irradiated with 3 MeV alpha particles at a grazing angle of 78 degrees. The implantation was performed in a continuous manner over a period of approximately 6 hours. Since the final optic experiences only a very minor temperature excursion (10's of degrees), continuous irradiation is an appropriate approach. A total alpha fluence of nearly 3×10^{17} cm^{-2} was achieved. This fluence is equivalent to 1-4 days of IFE exposure for a final optic stand-off of 15-30 meters, respectively.

Initial results showed discoloration, significant surface roughening, and a dramatic decrease in the reflectivity of the exposed region. Figure 2.3.1.1 shows a surface map of the

mirror before and after implantation. Figure 2.3.1.2 shows the reflectivity measured at several locations within the exposed region.

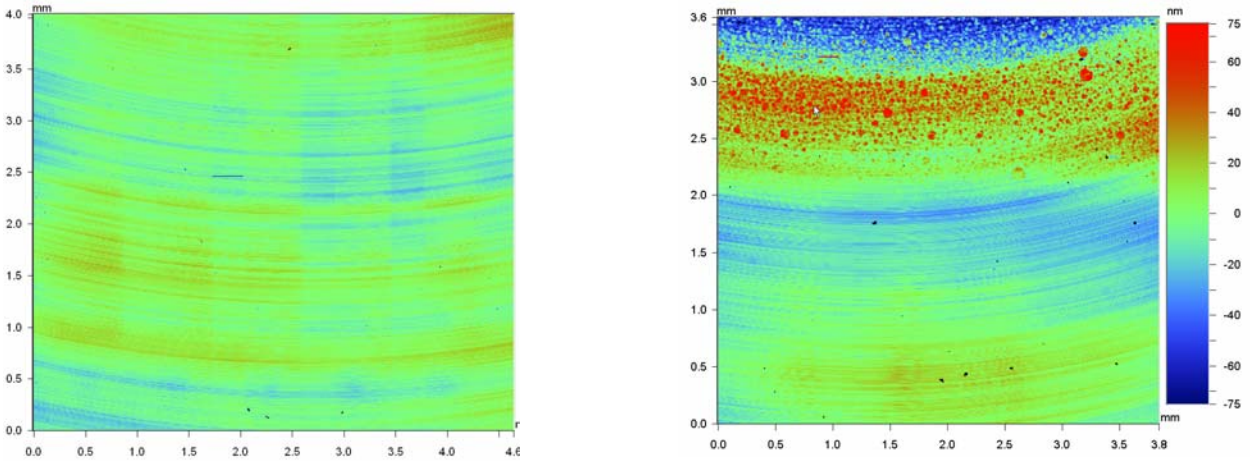

Fig. 2.3.1.1 White-light interferometer mapping of the UCSD mirror shows a surface that is initially quite smooth (left image) but is significantly roughening within the exposed region (top portion of right image).

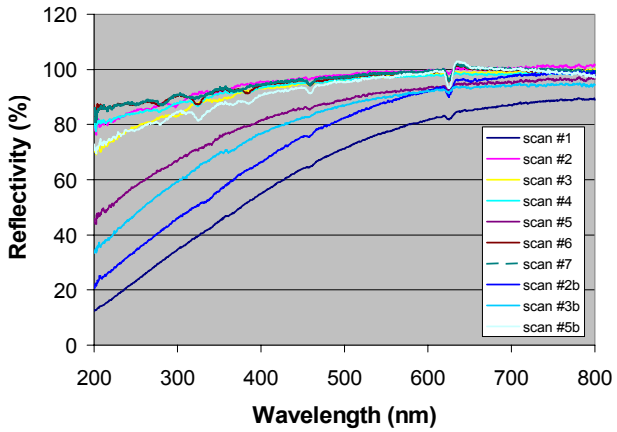

Fig. 2.3.1.2 Spectrophotomer measurements indicate significant changes in the reflectivity of the exposed region.

Fortunately, it was later realized (at the very end of FY2004) that the observed changes can be explained by an inadequate level of vacuum during the implantation process. Organics within the vacuum system (e.g., oils from pumps) were broken down by the alpha particle beam, and they coat the surface of the mirror. The apparent bubbles in Fig. 2.3.1.1 are actually particles that have been deposited upon the surface. FY2005 implantation runs already are utilizing a cryogenic pumping system to eliminate concerns about organic contamination.

2.3.2 Ion Debris Mitigation Study

Our FY2004 tasks were to:

- Include production of neutrals in our analysis of the ion deflection concept
- Implement ion straggling into the DEFLECTOR code
- Couple DEFLECTOR results to a heat transfer code and determine the heating effects of ions impacting final optics
- Explore the deflection system parameter space to identify acceptable magnetic field strengths and extents.

The threat from neutrals was determined to be negligible. A code called LISE was used to evaluate the neutral fraction of light ions at 8 m from chamber center (where the deflecting magnets will be placed) for typical target output spectra. Figure 2.3.2.1 shows typical results where neutral fractions over the range of significant energies for helium are no more than 10^{-5}. Predictions of neutral fractions for the other ion species (deuterium, tritium, etc.) were comparable. Assuming these small fractions of target output ions traverse the deflecting magnetic fields is highly conservative as these are equilibrium statistics. In reality, while 10^{-5} of the ions may be neutral at any given time, the mean free path in 10 mTorr xenon gas is on the order of 0.1 mm meaning no single ion will be neutral for any significant distance. This means that all ions will be deflected by the magnetic fields and any deviation from DEFLECTOR predictions due to this affect will be vanishingly small.

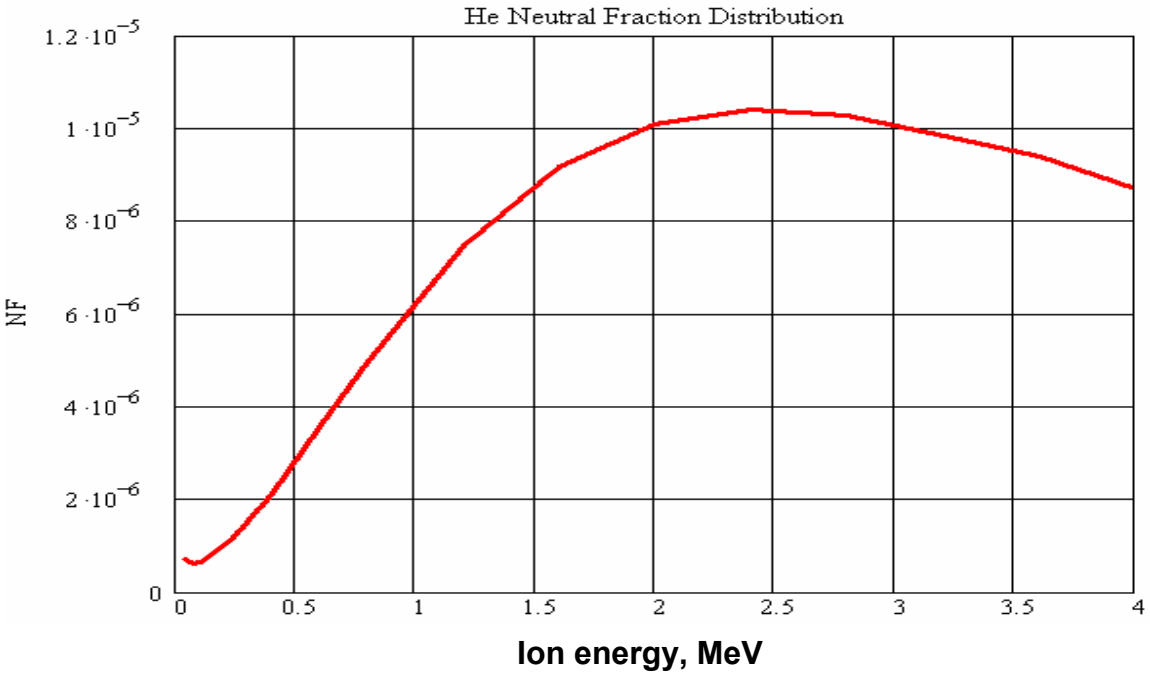

Fig. 2.3.2.1 Fraction of Helium ions expected to be neutral (NF) at relevant energies (in MeV).

Straggling (the lateral movement of ions due to collisions) was not implemented into the DEFLECTOR code as further simulations have shown that all ions can be deflected with modest fields such that they miss hitting final optics by several meters.

Automatic coupling of DEFLECTOR results to a heat transfer code that can handle ion irradiation (such as RadHeat) was deferred for several reasons. First, since the beam tubes upon which deflected ions will deposit can be made as robust as the tungsten first wall and the ions will be spread out over a greater area, it can be concluded that beam tube wall loading will not be an issue. Second, since all ions can be deflected from the final optics, heating of these components will be dominated by other target emitted radiation such as neutrons and photons. Finally, it would be relatively easy to engineer beam dumps in the regions of the beam tubes that experience the highest temperatures and/or stresses. Future work will identify these regions and manual RadHeat calculations will be completed to determine the extent of the issue.

Final optic contamination from sputter products due to ions impacting the beam tube wall was identified as a threat that warranted more in-depth consideration and analysis. The DEFLECTOR code was upgraded to determine the beam-tube impact angle and energy for all target output ions. Figure 2.3.2.2 shows examples for helium and gold. These results were then used by SRIM to quantify the number and range of sputtering products that could be expected. The range of the sputtered products was also determined assuming 10 mTorr of xenon within the beam tubes. Table 2.3.2.3 summarizes the results for gold. Further work needs to be done to quantify the threat from helium, carbon, and hydrogen.

A rough analysis of what an ion deflection would cost was carried out to gauge its significance in relation to other plant systems. A system of 120 copper coils for 60 beam-lines would consume approximately 10 MWe with materials for all magnets costing on the order of $2M.

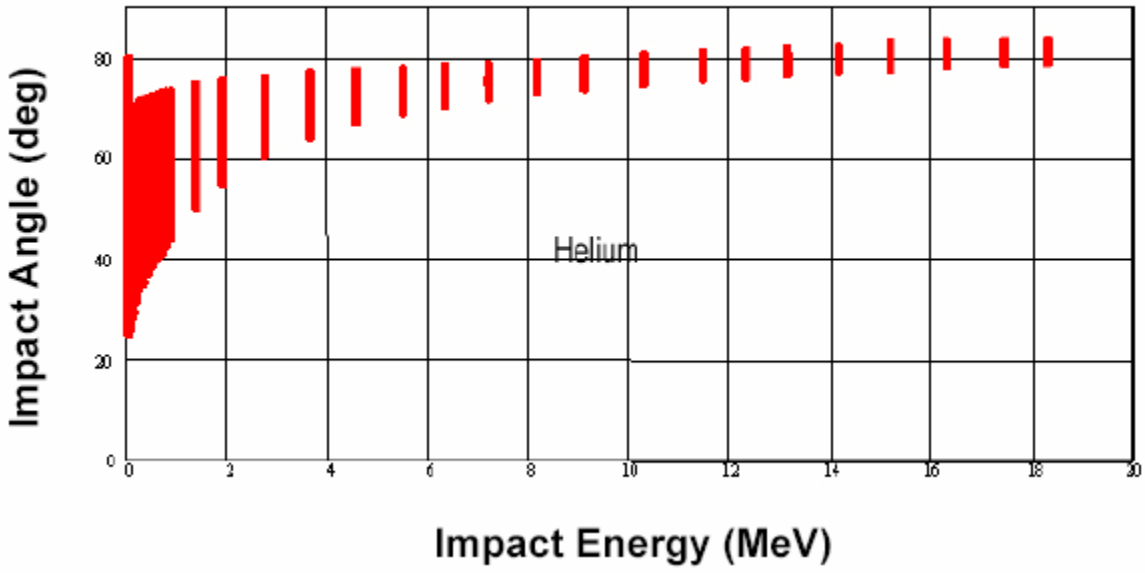

Fig. 2.3.2.2a Impact angle (degrees) for helium ions versus impact energy (MeV).

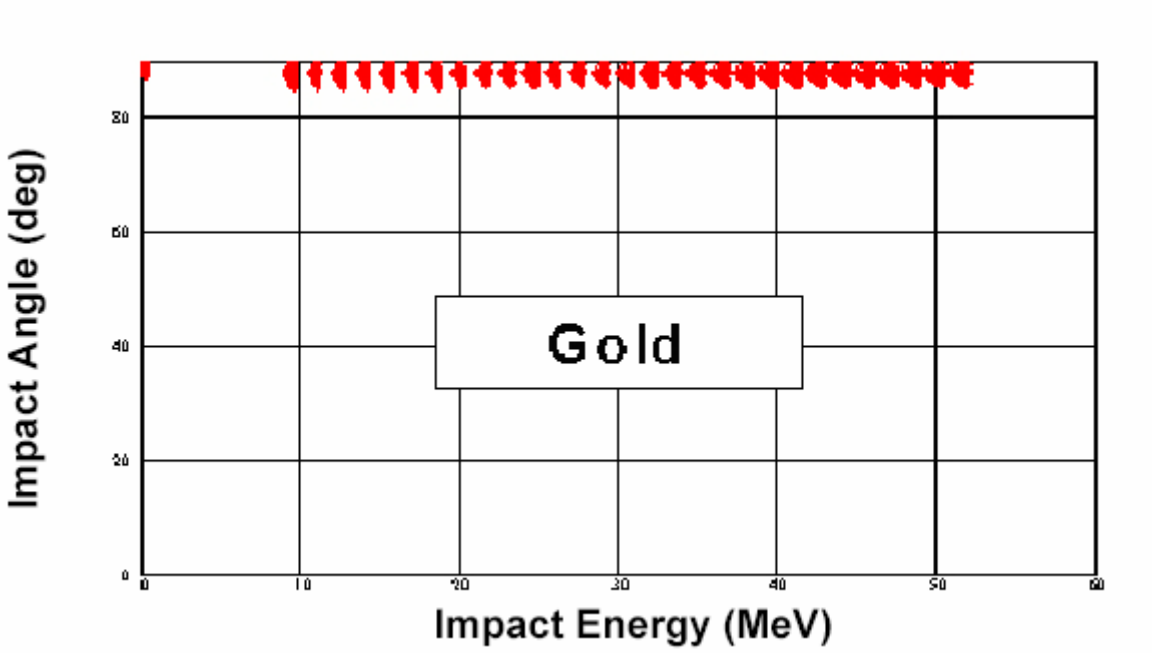

Fig. 2.3.2.2b Impact angle (degrees) for gold ions versus impact energy (MeV).

Table 2.3.2.3 Sputtering products from deflected gold ions.

Gold Ion Energy (MeV)	Impacts @ > 88°	Yield for Iron (atoms/ion)	Average Atom Energy (keV)	Range in 10 mTorr Xe (m)	Number of Sputtered Atoms
0 - 5	1.8×10^{11}	120	3.0	0.34	2.2×10^{13}
5 - 20	2.0×10^{12}	160	4.5	0.41	3.1×10^{14}
20 - 35	3.7×10^{10}	150	5.0	0.43	5.4×10^{12}
35 - 50	5.9×10^{6}	180	5.0	0.43	1.1×10^{9}

2.4 X-Ray Damage Studies

Our FY2004 tasks were:

- Complete x-ray exposure campaigns for tungsten, culminating in a run of 10^6 pulses for the armor selected in the First Wall Battle Plan.
- Begin x-ray exposures for aluminum mirrors to establish an acceptable operating window.
- Further develop the *in-situ* laser diagnostic.

During FY2004, a series of x-ray exposures were completed for various types of tungsten. The First Wall Battle Plan has yet to decide upon the details of an armor material, and thus, samples are not yet available for testing. X-ray exposures were completed for both single crystal and powder metallurgy tungsten for as many as 10^5 pulses. Tungsten foam samples were irradiated as well.

The first high-quality ellipsoidal condensing optic for XAPPER was produced, and the resulting x-ray fluence was high enough to melt tungsten with just a single shot (greater than 1 J/cm^2 with an average energy of 113 eV). Figure 2.4.1 shows scanning electron microscope (SEM) images of tungsten before and after exposure to 9000 pulses (delivered at 10 Hz) of approximately 1 J/cm^2. Note that the exposed sample shows stress cracking and appears to have grains popping out of the surface.

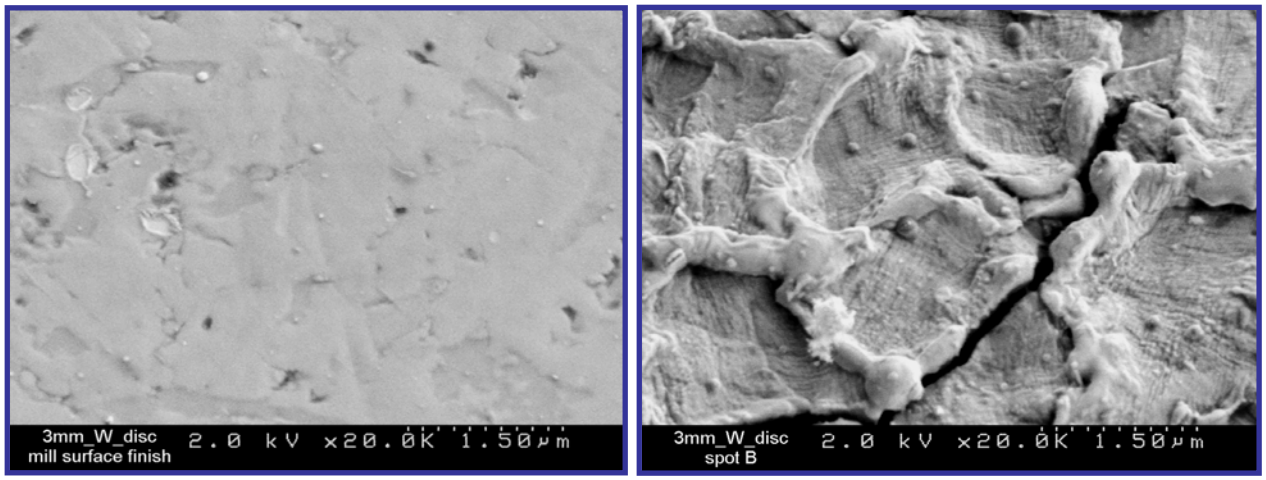

(a) (b)

Fig. 2.4.1 Image (a) shows unexposed tungsten, while image (b) shows tungsten that was exposed to 9000 pulses of approximately 1 J/cm^2.

Aluminum samples have been irradiated as well, although not at low enough x-ray fluences to be relevant for testing of IFE final optics. Figure 2.4.2 shows SEM images obtained for aluminum samples that were irradiated at 0.66 J/cm^2.

Using a custom chamber lid, a retrofitted camera tray and a borrowed CCD camera, the first images of the x-ray beam profile at focus were obtained. These images confirmed spot profile calculations and damage observations with spot sizes of 2 mm with the focusing optic in the original configuration and 1 mm with it in the reversed configuration. Following that series of experiments, a decision was made to procure a camera for everyday use on XAPPER. Figure 2.4.3 shows a typical spot with the focusing optic in the reversed configuration.

(a) (b) (c)

Fig. 2.4.2 Image (a) shows unexposed aluminum, while images (b) and (c) show regions that were treated with a single shot and 1000 shots at 0.66 J/cm^2, respectively.

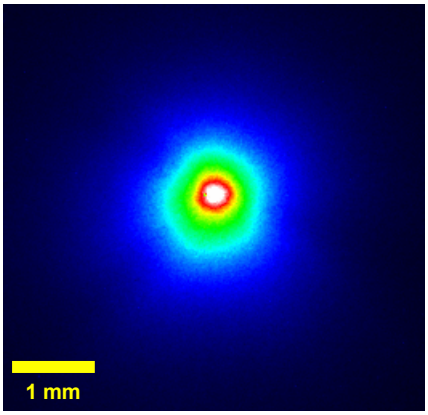

Fig. 2.4.3 A spot diameter of approximately 1 mm is observed with the focusing optic in the reversed configuration.

In order to facilitate additional diagnostics, such as the non-contact optical thermometer (designed and built by UCSD), a permanent CCD imaging system and the *in-situ* laser diagnostic, it was necessary to design and procure a larger chamber for XAPPER. This was completed in April 2004 as shown in Fig. 2.4.4a. The new chamber provides approximately 5× the volume of the old chamber. Figure 2.4.4b shows how the *in-situ* laser diagnostic will be fielded.

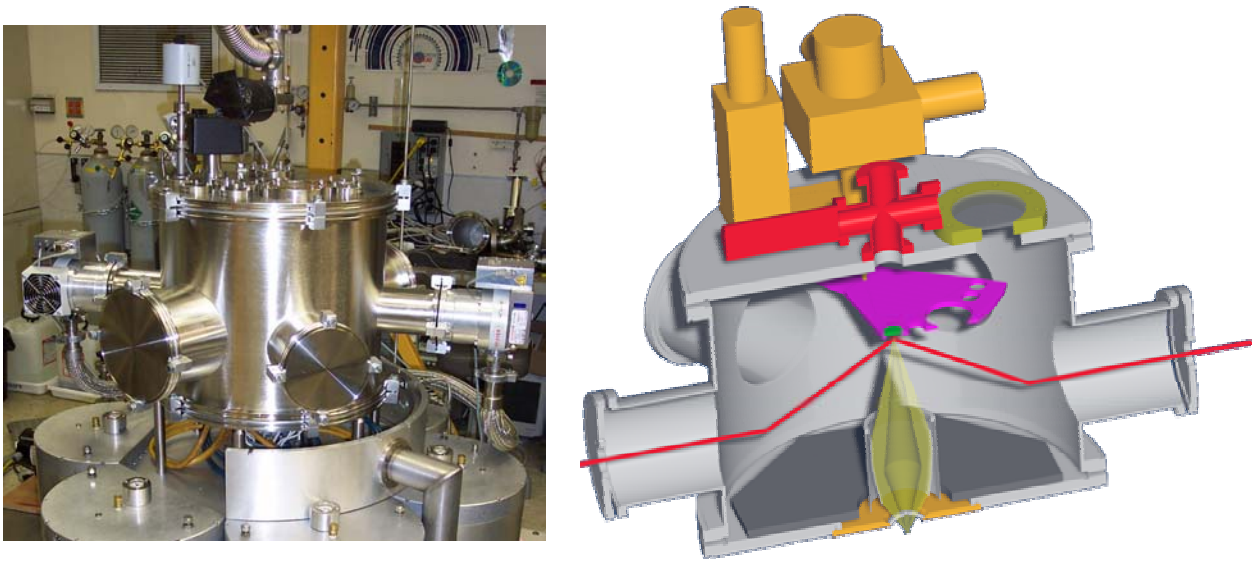

(a) (b)

Fig. 2.4.4 A new chamber was installed in April 2004. The new chamber facilitates increased diagnostic access, including the *in-situ* laser diagnostic, which is shown in the right CAD drawing.

In operating XAPPER, our goal has been to replicate the peak surface temperatures that would be expected in an actual IFE power plant. Naturally, this requires calculation of said temperature for both the IFE and XAPPER cases. This has been accomplished with our RadHeat chambers code, which was described in Section 2.2.1. Figure 2.4.5 shows a calculation of the time-temperature history for tungsten armor in the IFE chamber. Figure 2.4.6 shows the matching XAPPER case, which requires a fluence of 0.7 J/cm^2. Note that the XAPPER estimate assumes unheated samples. For samples heated to 600 ºC, a lower fluence would be required.

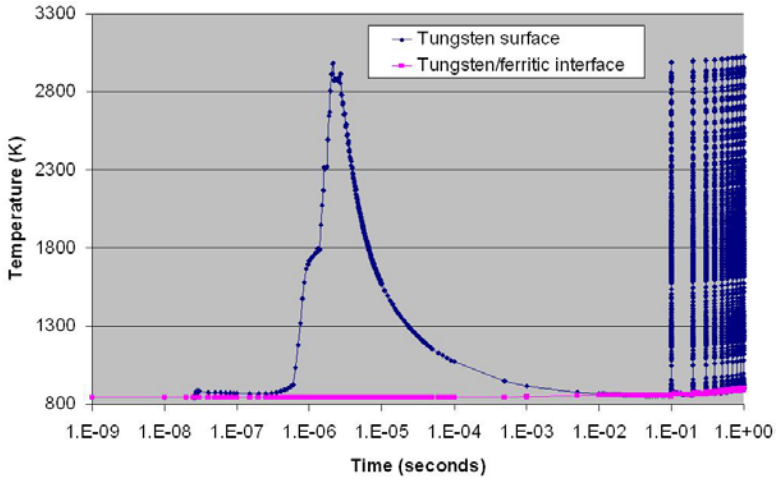

Fig. 2.4.5 With 10 mTorr of xenon gas, the 154 MJ target results in a peak temperature of approximately 2900 K for the surface of an 8-m-radius tungsten chamber.

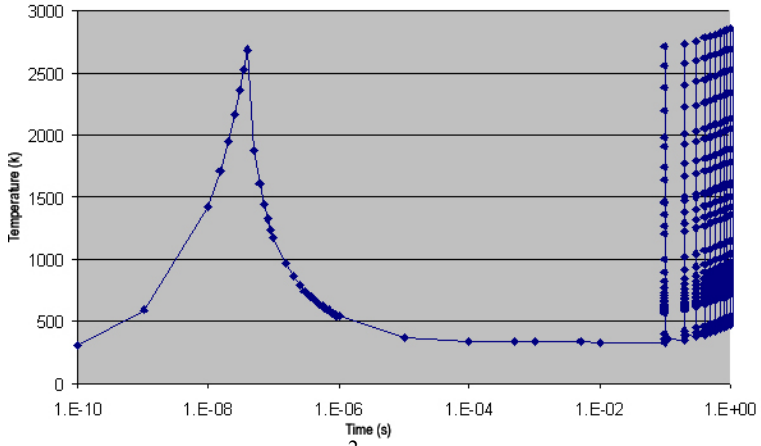

Fig. 2.4.6 With an x-ray fluence of 0.7 J/cm^2, XAPPER can provide a peak surface temperature that matches that calculated for the IFE case.

Powder metallurgy and single crystal tungsten samples were irradiated with an x-ray fluence of approximately 0.7 J/cm^2. Surface roughness was measured before and after irradiation using a Veeco white-light interferometer. Prior to irradiation the single crystal samples had an average surface roughness of approximately 10 nm, while that of the powder met samples was approximately 20 nm. The powder met sample was exposed to as many as 10^4 pulses, while the single crystal sample received as many as 3×10^4 pulses. Interestingly, the single crystal sample did not appear to roughen until after 3×10^4 pulses, yet it reaches the same surface roughness seen in the powder met sample after only 10^4 pulses (approximately 70 nm). Figure 2.4.7 shows the measured surface roughness for each material as a function of the number of pulses.

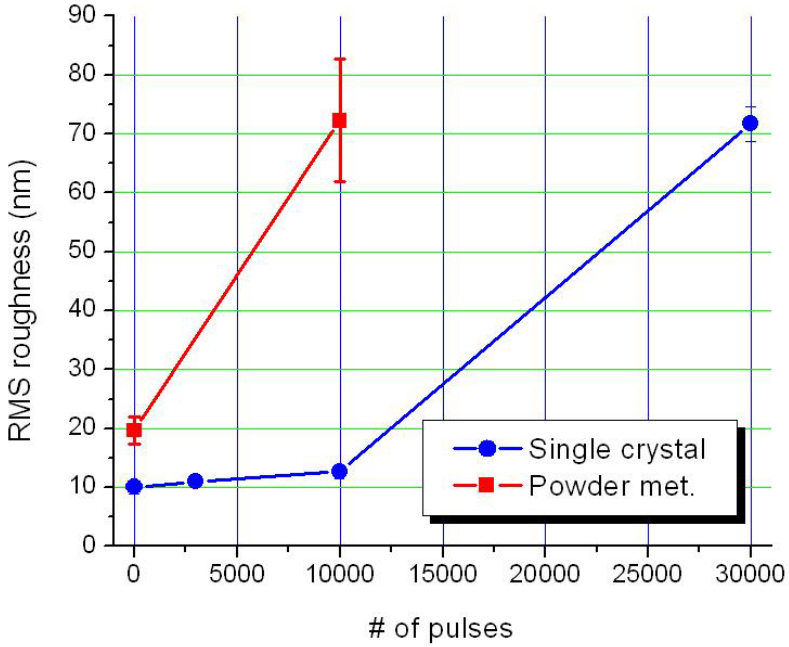

Fig. 2.4.7 The surface roughness has been measured for two types of tungsten as a function of the number of pulses at 0.7 J/cm^2.

Some questions that arise from the surface roughness data include:

- Will the roughening continue to grow or will it saturate?
- Will the roughening of each type of material grow at the same rate?
- Is the roughening curve repeatable?
- What level of roughening is acceptable for an IFE first wall?

A significant achievement during FY2004 is the development of a method to measure the x-ray fluence on XAPPER. Previously, a photodiode was used behind a pinhole. Unfortunately, this method proved to be unreliable due to the fact that the beam reaches focus from a variety of angles. For example, with the optic in the reversed configuration, photons that arrive at the bottom of the optic are imaged 1:1 to the sample. These photons have a 15-degree angle of incidence relative to the pinch axis. Photons that reflect off the top portion of the optic, however, are demagnified by 4:1. These photons arrive with a 31-degree angle of incidence. Since they are demagnified, they contribute the highest level of fluence per unit solid angle. It is very important to capture the wide-angle portion of the beam in order to make an accurate measure of the fluence. Unfortunately, this requires a rather large pinhole, which then allows too much energy to arrive from the low-angle portion of the beam. This saturates the detector.

One can consider the use of an x-ray filter to allow a larger pinhole without saturating the detector, but this is not practical for a number of reasons. First among these is the fact that filtering must be performed far from focus. XAPPER is, after all, capable of melting tungsten in a single shot. The level of filtering that is needed is factors of 2-5×. Second, such filters are extremely thin (hundreds of nanometers), and thus, very fragile. They are also quite expensive for a large aperture. Finally, the filter cannot be used as an absolute measure for long, as debris from the plasma head quickly coats the filter leaving its degree of attenuation unknown.

Instead, our approach has been to separate the measurement of beam profile from energy. Images provided by the CCD camera are used to establish the beam profile. This data is combined with calorimeter energy measurements to determine the peak x-ray fluence. The CCD camera uses a relatively thick (4 μm) zirconium filter, which is robust enough that the material can be cut by hand with scissors. The Zr sheets are relatively inexpensive and may be tough enough to be cleaned when debris builds up to an unacceptable level. The calorimeter is configured with a relatively large (6.35-mm-diameter) aperture that sits at focus. After passing through focus at the aperture, the beam is allowed to expand to approximately 1-cm-diameter before striking the active region of the calorimeter. This ensures that the x-ray fluence is low enough that the calorimeter is not quickly damaged.

This method has proven useful in measuring the x-ray fluence up to repetition rates of 1-2 Hz. Higher speed measurements may require a higher speed imaging system. Discussions suggest that such a system might be possible without great expense. It is expected that such a system will be implemented during FY2005.

2.5 Direct-Drive Target Design

Design and Performance

We have evolved the design and performance of high yield direct-drive targets for inertial fusion energy, driven by both KrF (0.25 μm) and DPSSL (0.35, 0.5 μm) lasers. The baseline design studied in FY2004 is shown in Fig. 2.5.1. It is characterized by 150 μm of 1000 mg/cc "empty" foam on the outside to thermally insulate the cryogenic fuel and ablator from heating via buffer gas friction and first wall thermal radiation.

The drive pulse shape is distinguished by a high intensity "picket" prepulse to set the ablator on a high adiabat and thus enhance its Rayleigh-Taylor stability through increased ablation velocity. In particular, at spherical mode numbers around 100, growth factors gave been reduced from approximately 100,000 to only approximately 300. However, note from Fig 2.5.1 that we have traded some gain for this increased stability.

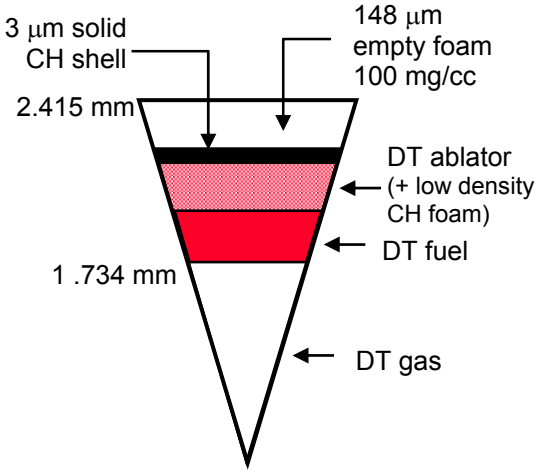

	Picket Pulse	Standard Pulse
Yield (MJ)	343	384
E_{laser} (MJ)	2.94	2.44
Gain	117	157
Max ρR (g/cm^2)	2.22	2.86
Velocity (cm/s)	3.25x10^7	2.99x10^7
In-flight adiabat α_{IF}	2.31	1.65
Shell breakup fract	0.15	1.8

Fig. 2.5.1 High gain insulated foam target design.

Understanding Compression, Ignition and Burn in High Gain Targets

Observations of full rad-hydro-burn simulations of our direct-drive high-gain target designs for HAPL show that the common wisdom of isobaric (constant pressure) conditions around stagnation/ignition is incorrect. In particular, at ignition:

1) The hotspot and cold fuel are not in pressure equilibrium (even under "burn-off" conditions);
2) The fusion alpha energy produced up to this time can exceed the P-dV work supplied from the stagnating shell and, therefore, must be included in any modeling of energy and pressure balances;
3) The cold fuel partitions into a stagnated tamp mass and a still-ingoing unstagnated portion; the latter carries a substantial fraction of the total ingoing mass and rho-R;
4) These two cold fuel regions are not sonically coupled at ignition, thus only the decreasing tamp momentum balances the hotspot pressure;
5) The hotspot criteria for ignition (T_{hot}_req'd, rhoR_{hot}_req'd) are not fixed constants but depend on the tamp conditions.

We conclude that hotspot formation, ignition and burn are dynamic processes such that even zero-dimensional models must be time-dependent to provide an adequate description of the physics. Accordingly, we have formulated a fully dynamic 0-D model based on six coupled ordinary differential equations that describe energy, momentum and mass balances across the hotspot/cold fuel system [1].

We are now able to obtain fast (approximately 10s) accounting of the processes through compression, stagnation, ignition and burn, including full thermonuclear energy production under burn disassembly. Very good agreement with 1-D simulations is obtained for integral quantities such as gain, yield and ignition margins. The new O-D model is now being applied to aid in the design optimization of future targets and for scoping design space for direct-drive gain curves.

Future Work for FY2005

1) Commence full 2-D stability analyses for insulated-foam, direct-drive target design with full beam geometry.
2) Produce a formal set of gain curves for direct-drive with laser frequency as a parameter (2, 3 and 4ω).
3) Extend our new non-isobaric 0-D target model and apply to (a) understanding direct drive target design issues (b) scoping direct drive gain curves and (c) performing target optimization.
4) Determine target output (threat) spectra – burn products, x-rays and thermal debris – for use in chamber damage studies.

Publications

[1] L.J. Perkins, M.Tabak, "Dynamic Models for the Compression, Ignition and Burn of ICF Targets", *Bull. Amer. Phys. Soc.* **46** 61 (2004).

FY2005 STATEMENTS OF WORK AND DELIVERABLES

Task 1.0 DPSSL Development

Task 1.1 Fabricate Yb:S-FAP Crystals

Continue fabrication and growth of gain media for Mercury laser both at LLNL and commercial facilities. Produce coated and characterized slabs for the laser system.

Task 1.2 Full System Activation with Two Yb:S-FAP Amplifiers

Activate system with two gas cooled amplifiers and wavefront correction for average powers of greater than 250 W at 1.047 μm. Diagnose performance with a suite of diagnostic packages to measure spatial, temporal, and energy characteristics. Benchmark codes with data

Task 1.3 Advanced Technologies

Develop broadband injection laser with temporal and spectral capabilities. Design, build and demonstrate frequency conversion hardware and do integrated tests at 2ω on the Mercury Laser.

Task 2.0 Chambers

Task 2.1 Chamber Response & Safety and Environment

Continue with development and utilization of the RadHeat code and provide safety and environmental support to design integration activities. Implement finite element and stress-strain models within RadHeat and design shielding layout for the "droopy cusp" magnetic protection scheme.

Task 2.2 Systems Modeling and Design Integration

Continue development of scaling relationships for fusion chambers, blankets and power conversion systems. Incorporate new KrF and DPSSL models (developed by laser designers) into the laser IFE systems code. Assist in the development of an integrated design concept.

Task 3.0 Final Optics

Task 3.1 Irradiation Studies

Continue ion and neutron irradiations studies for grazing incidence aluminum metal mirrors with emphasis on threshold for ion implantation damage in aluminum mirrors.

Task 3.2 Ion Debris Mitigation Study

Continue modeling and design activities for a magnetic system to protect the final optics from burn and debris ion damage. Provide self-consistent parametric results for a variety of ion deflection options for protection of the final optics.

Task 4.0 X-ray Damage Studies

Task 4.1 X-ray Damage Studies

Continue x-ray exposures and modeling for single crystal and powder metallurgical tungsten samples. Begin x-ray exposures for candidate final optic materials. Generate x-ray damage and roughening data for multiple varieties of heated and unheated tungsten, including several x-ray fluences and numbers of pulses.

Task 5.0 Target Design

Task 5.1 Foam-Insulated Target Design

Perform 1-D design optimization studies and 2-D stability analyses of this target to obtain a recommended baseline design.

Task 5.2 Dynamic 0-D Models for Compression, Ignition and Burn

Continue the development of a new dynamic 0-D model for compression, ignition and burn. Complete Mathematical model for dissemination plus results from application to target gain curves and target gas fill.

Task 5.3 Optimization of DPSSL-Driven Targets with Frequency

Continue trade-off studies that will be used to determine the best DPSSL laser frequency by optimizing target and driver performance.

Task 5.4 Target Performance Parameters and Output Threat Spectra

Calculate target performance parameters (e.g., gains, yields, etc.) and target output (threat) spectra (burn products, x-rays and thermal debris). Disseminate target output results for use by other groups in chamber, optics and systems design studies.

FY2005 COST BY ELEMENT

1.0	**DPSSL Development (Subtotal = $8,387,000)**	
1.1	**Fabricate Yb:S-FAP Crystals**	**$1,912,000**
1.2	**Full System Activation with Two Yb:S-FAP Amplifiers**	**$3,736,000**
1.3	**Advanced Technologies**	**$2,353,000**
1.4	**Operations Overhead**	**$386,000**
2.0	**Chambers (Subtotal=$203,000)**	
2.1	**Chamber Response & Safety and Environment**	**$88,000**
2.2	**Systems Modeling and Design Integration**	**$115,000**
3.0	**Final Optics (Subtotal=$363,000)**	
3.1	**Irradiation Studies**	**$288,000**
3.2	**Ion Debris Mitigation Study**	**$75,000**
4.0	**X-ray Damage Studies (Subtotal=$567,000)**	**$567,000**
5.0	**Target Design (Subtotal=$280,000)**	**$280,000**
TOTAL		**$9,800,000**

TECHNICAL CONTRIBUTORS TO THIS PLAN

Lawrence Livermore National Laboratory
- Ryan Abbott (Chambers, Final Optics, X-ray Damage)
- Paul Armstrong (Front End Laser)
- Andy Bayramian (Laboratory experiments)
- Ray Beach (Diodes, IRE)
- Camille Bibeau (Mercury Project Leader)
- Chris Ebbers (Front End, Editor)
- Alison Kubota (Molecular Dynamic Simulations)
- Jeff Latkowski (Chambers, Final Optics, X-ray Damage)
- Zhi Liao (Wavefront Control)
- Wayne Meier (Chambers, Systems Modeling)
- Joe Menapace (MRF Phase Plate Technology)
- John Perkins (Target Design)
- Susana Reyes (Safety and Environment)
- Kathleen Schaffers (Crystal Growth)
- Steve Telford (Control System)
- LLNL Managers:
- Ed Moses (Associate Director for the National Ignition Facility)
- Wayne Meier (Deputy Program Leader for IFE)

Point of Contacts:

Coherent, Inc. (Diodes)
- Paul Rudi

Northrop Grumman (Crystals)
- Mark Randles

Onyx Optics, Inc. (Diffusion Bonding)
- Oliver Meissner

Directed Energy Inc. (Pulsers)
- Ron Sherwood

Schott Technologies
- Joe Hayden

PLEX LLC
- Malcolm McGeoch